Computers and Geotechnics 49 (2013) 226–244

Contents lists available at SciVerse ScienceDirect

Computers and Geotechnics

journal homepage: www.elsevier.com/locate/compgeo

Microcrack-based coupled damage and flow modeling of fracturing evolution in permeable brittle rocks

Y.L. Lu [a,b,*], D. Elsworth [b], L.G. Wang [a]

[a] State Key Laboratory for Geomechanics and Deep Underground Engineering, China University of Mining and Technology, Xuzhou, Jiangsu 221008, People's Republic of China
[b] EMS Energy Institute, G3 Center and Energy and Mineral Engineering, Pennsylvania State University, University Park, PA 16802, USA

ARTICLE INFO

Article history:
Received 12 September 2012
Received in revised form 23 November 2012
Accepted 27 November 2012
Available online 21 December 2012

Keywords:
Microcracks
Damage
Hydro-mechanical coupling
Finite element method
Hydraulic fracturing

ABSTRACT

Microcracks in brittle rocks affect not only the local mechanical properties, but also the poroelastic behavior and permeability. A continuum coupled hydro-mechanical modeling approach is presented using a two-scale conceptual model representing realistic rock material containing micro-fractures. This approach combines a microcrack-based continuous damage model within generalized Biot poroelasticity, in which the tensors of macroscopic elastic stiffness, Biot effective stress coefficient and of overall permeability are directly related to microcrack growth. Heterogeneity in both mechanical and hydraulic properties evolves from an initially random distribution of damage to produce localized failure and fluid transmission. A significant advantage of the approach is the ability to accurately predict the evolution of realistic fracturing and associated fluid flow in permeable rocks where pre-existing fractures exert significant control. The model is validated for biaxial failure of rock in compression and replicates typical pre- and post-peak strength metrics of stress drop, AE event counts, permeability evolution and failure modes. The model is applied to the simulation of hydraulic fracturing in permeable rocks to examine the effects of heterogeneities, permeability and borehole pressurization rate on the initiation of fracturing. The results indicate that more homogenous rocks require higher hydraulic pressure to initiate fracturing and breakdown. Moreover, both the fracturing initiation pressure and breakdown pressure decrease with permeability but increase with borehole pressurization rate, and the upper and lower limit of the initiation pressure are seen to be given by the impermeable (Hubbert–Willis) and permeable (Haimson–Fairhurst) borehole wall solutions, respectively. The numerical results are shown to be in good agreement with the experimental observations and theoretical results. This coupled damage and flow modeling approach provides an alternative way to solve a variety of complicated hydro-mechanical problems in practical rock engineering with the process coupling strictly enforced.

1. Introduction

The role of fluids in the fracturing of crustal rocks is well established and is fundamental to a variety of geological and engineering processes. These include forecasting the integrity of reservoirs for underground CO_2 sequestration or hazardous waste storage, preventing water/gas outbursts into underground mines and improving and optimizing hydraulic fracturing for well stimulation in low permeability reservoirs [1], among others. The massive hydraulic fractures produced in rocks during artificial stimulation of underground reservoirs exert a profound influence on various key mechanical and transport properties of the rock, including the elastic modulus, anisotropy, elastic wave velocities and permeability [2,3]. Therefore, an adequate understanding and quantification of the fracture evolution and associated fluid flow behavior in rock is of great importance and has a vital role in applied science and engineering of the subsurface.

With the aid of microscopic observations (e.g. SEM, X-ray CT, etc.) it is clear that fracture evolution in rock is a process of progressive damage accumulation [4–6]. This is characterized by the initiation, growth and coalescence of numerous microcracks, as a result either of change in the external load or of a change in the internal pore fluid pressure. However, such complex mechanisms of microfracturing are very difficult to describe faithfully. A variety of models intended to accommodate these microscopic mechanisms have evolved to reproduce the macroscopic behavior of rocks (for comprehensive reviews, see Refs. [7,8]). In general, process-based computational models for simulating fracturing in rock can be classified into two categories, depending on whether damage is represented *directly* by tracking the evolution of numerous microcracks or *indirectly* by its effects on the phenomenological

* Corresponding author at: State Key Laboratory for Geomechanics and Deep Underground Engineering, China University of Mining and Technology, Xuzhou, Jiangsu 221008, People's Republic of China. Tel.: +1 814 232 2819.
E-mail address: yinlong_lu@163.com (Y.L. Lu).

0266-352X/$ - see front matter © 2012 Elsevier Ltd. All rights reserved.
http://dx.doi.org/10.1016/j.compgeo.2012.11.009

constitutive relations [9]. Specifically, in *direct* approaches [10–15] rock material is discretised into a collection of idealized microstructural units (such as springs, beams or particles) and fracturing is represented by the breakage of these individual microscopic units. Conversely, in the *indirect* approach [16] rock is idealized as a continuum with material degradation in constitutive relations to represent irreversible microstructural damage. Continuum damage mechanics (CDM) which is capable of reproducing the degraded macroscopic properties of rock material is widely applied in this indirect approach.

Computational models based on the indirect approach (CDM) are becoming progressively more sophisticated. Typical capabilities of such models [17,18] include the incorporation of initial heterogeneous stiffness and strength of individual basic elements that are allowed to degrade based on a simple strength failure criterion in the form of an elastic-brittle constitutive relation, yet most models following the indirect approach assume the rock to be impermeable [8,19] and the effects of hydro-mechanical coupling on fracturing behavior are typically neglected. However, in many situations this H–M coupling is *the essence* of the interaction and accommodating these effects is crucial if accurate description of processes is to be accomplished. Such coupled numerical models have found limited development and are briefly reviewed here. Tang et al. [20] proposed a flow-stress-damage coupling model for heterogeneous rocks. This model was implemented within a previously developed code for rock failure process analysis (RFPA) [17] and used to investigate the evolution of damage and fluid flow. Yuan and Harrison [21] extended a local degradation approach [18] to include the hydro-mechanical behavior through the introduction of elemental models for dilatancy and permeability. More recently, Lyakhovsky and Hamiel [22] presented a thermodynamically based continuum poroelastic damage model for simulating the coupled evolution of fractures and fluid flow in poroelastic rock. However, these models are all under the framework of phenomenological damage theories. The damage evolution equations in these models surrender insightful descriptions of microstructural microcrack kinetics. Such relevant micromechanics features are of particular importance for modeling the connectivity and flow characteristics of rock and should be incorporated in the coupled fracturing and flow modeling of rock [23].

Following the indirect approach, a major difficulty in the modeling of coupled fracturing and fluid flow is of how to link the elastic properties, poroelastic properties and permeability to the growth of damage. Experiments observe that there can be significant evolution of elastic modulus, Biot effective stress coefficients and permeability with the growth of microcracking [24,25]. The traditional phenomenological damage models are formulated on a somewhat heuristic basic, rather than on the microscopic kinetics of microcrack growth, so it remains difficult to evaluate accurately the mechanical and hydraulic properties of rock as a function of damage evolution. To overcome the disadvantages encountered in the phenomenological damage models, one alternative is to develop continuous damage models based on the results of microscopic analyses. Costin [26] originally proposed a microcrack-based continuous damage model by introducing a continuum damage surface to represent microcrack propagation. This model was then further implemented into a specific finite element code to simulate the deformation and failure of brittle rocks [27]. Hommand-Etienne et al. [28] developed a similar damage model and implemented it in a discrete element code (UDEC) to investigate the characteristics of an excavation damaged zone (EDZ). However, hydro-mechanical coupling is not included in either of these models. Recently, Shao et al. [29,30] further developed the microcrack-based continuous damage model to link anisotropic poroelastic behavior and permeability to damage evolution in brittle rocks. These models facilitate better understanding of fundamental characteristics of coupled damage growth and fluid flow, but they have not been combined with numerical simulation techniques to further study the progressive fracturing and associated flow behavior of permeable rocks under complex hydro-mechanical loading conditions. A notable exception is where an anisotropic microcrack-based damage model [31] was extended to account for changes in permeability around an underground research laboratory, although the evolution of explicit fracturing is not incorporated in this model.

In the following, we present a coupled microcrack-based damage and flow modeling approach in the framework of a continuum numerical method. This focuses on understanding the fundamental processes of progressive fracturing and associated fluid flow in permeable rocks. The basic difference between the modeling approach presented here and some other approaches which incorporate damage and flow coupling behavior is that in the present approach the macroscopic elastic modulus tensor, Biot effective stress coefficient tensor and the overall permeability tensor are all directly related to the microcrack growth. This allows prediction of the evolution fracturing and flow in realistic fractured media where fracture-fluid interaction effects are important. In the following the principles of the numerical approach are presented (Section 2), the approach validated (Section 3) before being applied to the simulation of hydraulic fracturing (Section 4).

2. Numerical approach

In this section, we briefly describe the principles of the coupled damage and flow modeling approach in the framework of a continuum numerical method. A two-scale conceptual model is used to represent realistic rock material containing micro-fractures. This medium is assigned a microcrack-based failure criterion and initial damage with the resulting system of equations solved by a numerical approach.

2.1. Conceptual model

It is well known that brittle rocks are typically strongly inhomogeneous at a variety of length scales. Here, we make a preliminarily focus on rock at the laboratory length scale where the mechanical and hydraulic behavior is mainly controlled by grain-scale heterogeneity including grain boundaries, micropores and microcracks. However, such complicated textures are very difficult to replicate realistically in a numerical model. To aid a faithful mechanistic representation of these defects we assume that the macroscopic rock can be divided into a series of regularly arranged, uniform and square microscopic elements, i.e. representative elemental volumes (REVs), as shown in Fig. 1a. Such microscopic elements in conventional statistical models [15,17,18] are commonly assumed to be homogeneous and isotropic. This assumption, however, obscures the important micromechanical features in the REV, such as the distributions and evolution in length, aperture and density of microcracks. This microscopic information is particularly useful and essential for modeling the alteration of hydraulic properties (e.g. permeability) [30,32]. For this reason, in this paper it is assumed that each of the microscopic elements is not homogeneous but rather is a heterogeneous medium consisting of a rock matrix containing an arbitrary distribution of microcracks randomly oriented in space (see Fig. 1a). The matrix of the REV is assumed to be an equivalent isotropic homogenized porous medium which is composed of solid grain constituents and micropores. A family of idealized microcracks (line crack for 2-D and penny-shaped crack for 3-D) are inserted into this matrix, each of which can be specified by its initial length ($2a_0$) and orientation angle (β) in the case of the two-dimensional problem. Thus, the real rock

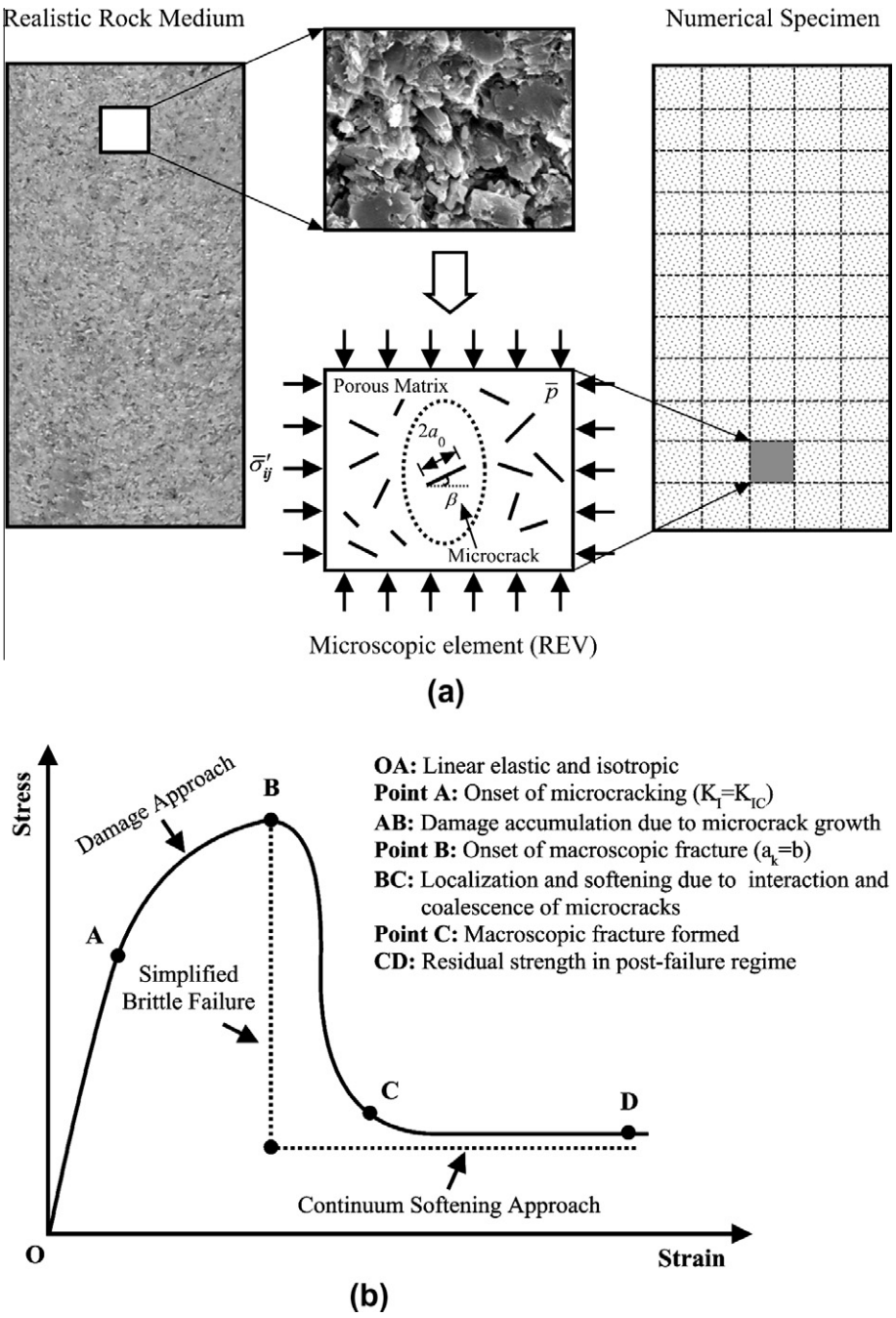

Fig. 1. (a) A two-scale conceptual model for the representation of realistic rock medium. a_0 and β are initial length and orientation angle of microcracks, respectively. $\bar{\sigma}'_{ij}$ and $\bar{p}$ are the average effective stress and pore pressure over the REV, respectively. (b) Schematic of typical stress–strain curves with corresponding transition from damage to failure for a microscopic element (after [18,33,34]). K_I and K_{IC} are the Mode I stress intensity factor and the Model I fracture toughness, respectively. a_k is the microcrack length and b is the critical length of microcrack which defines the failure of the microscopic element.

medium is then represented by a two-scale (micro–macro scale) conceptual model: (i) at macro-scale the rock medium is composed of the REVs and (ii) at micro-scale each of the REVs comprises both homogeneous porous matrix and distributed microcracks.

Physically, the failure process of rock includes three stages: linear elastic response, the evolution of damage with microcracks but without macrocracks, and then the combination of both microcracking and macrocracking [33]. In the framework of a continuum numerical method, the evolution of rock failure can be described by tracking the entire range of physical behavior of the microscopic elements (REVs) defined in the above two-scale model (i and ii). An individual REV may experience the processes of deformation, damage and failure similar to the macroscopic rock specimen in laboratory experiments [18], as shown in Fig. 1b. Initially, the REVs are considered to be elastic and isotropic, but the properties of these elements vary randomly from point to point within the rock. This results in heterogeneity of the medium at the macro-scale. Then, with an increase of the effective stresses applied to the REVs, damage by microcracking begins to accumulate. The accumulation of damage induces changes in the mechanical and hydraulic properties of the rock including the elastic stiffness, Biot effective stress coefficients, Biot modulus and permeability. The governing equations for describing such relations are presented in the following. Finally, as the microcracks in the REVs become so numerous and

necessarily closely-spaced that interaction among them is inevitable, the damage accumulation accelerates due to the unstable growth and coalescence of microcracks. This results in the localization of damage, strain softening response, and eventually the development of large scale fractures which imply the failure of the REVs [34]. After that, the failed REVs could still retain residual strength when they are subject to the confining pressure [18]. However, for simplicity, it is assumed in this paper that the macroscopic fracture is formed instantaneously (brittle failure) and a continuum softening law is employed to gradually degrade the properties of the failed REVs in the post-failure regime. When the failed REVs are subject to large tensile loading, macroscopic fracture surfaces will be formed in these failed elements and these surfaces will separate. To facilitate modeling this discontinuity, an extremely small magnitude of stiffness is applied to the completely failed REVs [35]. In this respect, the initiation and propagation of macroscopic fractures is simply simulated.

Actually, the above modeling approach originates from the smeared crack model [36] in conventional fracture mechanics analysis. Thus no special singular element is used for the finite element analysis, which simplifies the problem of the discontinuity since it requires no change in the mathematical description of the model. The macroscopic fracture has the width of a microscopic element (REV). The dimensions of the REV should be proportional to the smallest size of the damage localization zone or fracture process zone [33]. Quantitatively, Bažant and Oh [36] proposed that the size of such microscopic elements must be at least several times the maximum aggregate size in the case of concrete. Following this suggestion, the size of the REV in this paper is taken as 5–10 times the maximum length of microcracks for brittle rocks. Based on the two-scale model and the physical process of rock failure, it allows the modeling of the macroscopic fracturing behavior of rock as prescribed by processes at the microscopic level. This allows the tracking of the dynamic evolution of fracturing and fluid flow in permeable rocks by FEM in the framework of continuum mechanics.

2.2. Governing equations

Damage evolution, elastic properties, poroelastic properties and permeability are a function of the propagation of the microcracks. The following briefly summarizes the main governing equations for these features (for detailed derivations, see Refs. [28,30,37–39]). All the equations are established at the elemental scale (for the REV). The symbols used in the equations are summarized in Table 1.

2.2.1. Damage tensor and damage evolution law

The rock material considered in this study is assumed to be saturated. The REV is made of a homogenized porous medium with embedded random microcracks. Damage is relative, and virtually any state of damage can be considered as the reference state or initial state. Here, the state of the rock before loading is applied is regarded as the initial state and is defined as the "undamaged" state. The definition of the damage variable depends on the different modeling approaches that could be adopted [16]. In this paper, emphasis is placed on the influence of microcracks on hydro-mechanical coupling behavior. Therefore, a symmetric second-order damage tensor based on the relative variation of microcrack density within the REV [28,40] is followed. It is considered that N families of idealized line microcracks (for 2-D) or penny-shaped crack (for 3-D) are uniformly intersected in the REV. Each of the microcrack families is characterized by the unit vector $\mathbf{n}_k$, the statistical average length or radius a_k and the number density m_k which is defined by the ratio between the number of microcracks in family k and the volume of the REV. Thus, the microcrack damage tensor is:

$$\mathbf{D} = \sum_{k=1}^{N} m_k \cdot d_k \cdot (\mathbf{n}_k \otimes \mathbf{n}_k) \tag{1}$$

with $d_k = (a_k^3 - a_0^3)/a_0^3$ for the 3-D case and $d_k = (a_k^2 - a_0^2)/a_0^2$ for the 2-D case.

In these equations, a_0 denotes the average length of initial microcracks which is assumed to be uniform in the REV in the initial undamaged state, and d_k is the relative variation of microcrack density induced by microcrack growth.

According to the definition of Eq. (1), the evolution of the damage tensor is inherently related to the propagation of microcracks in each orientation. In fracture mechanics, there are two kinds of crack growth criteria [26]: mechanical growth (time-independent) due to stress variations and subcritical growth (time-dependent) due to stress corrosion. Here, only the time-independent crack growth is taken into consideration. Costin [26] first suggested that the driving force for microcrack propagation is local tensile stress which is a function of the macroscopic stresses applied and the microcrack orientation and formulated the criterion of microcrack propagation based on linear fracture mechanics. Moreover, Shao [37] extended this criterion to saturated brittle rocks to take into account the effect of pore pressure by using the concept of Terzaghi effective stress. Such a criterion is chosen in this paper as the damage evolution law:

$$K_{\mathrm{I}}(\boldsymbol{\sigma}, p, a_k, \mathbf{n}_k) = \sqrt{\pi a_k} \cdot \sigma_t = \sqrt{\pi a_k} \cdot [\sigma_n + p + f(a_k)\mathbf{n}_k \cdot \mathbf{S} \cdot \mathbf{n}_k] \tag{2a}$$

$$F(\boldsymbol{\sigma}, p, a_k, \mathbf{n}_k) = K_{\mathrm{I}}(\boldsymbol{\sigma}, p, a_k, \mathbf{n}_k) - K_{\mathrm{IC}} = 0 \tag{2b}$$

where K_{I} is the Model I stress identity factor of the microcrack, K_{IC} is the Model I fracture toughness, σ_t is the local traction on the microcrack in direction $\mathbf{n}_k$, $\boldsymbol{\sigma}$ is the total stress tensor, p is the pore pressure, $\sigma_n = \mathbf{n}_k \cdot \boldsymbol{\sigma} \cdot \mathbf{n}_k$ is the normal stress applied to the microcrack, and $\mathbf{S} = \boldsymbol{\sigma} - (tr\boldsymbol{\sigma}/3)\boldsymbol{\delta}$ is the deviatoric stress tensor. The scalar function $f(a_k)$ in Eq. (2a) defines a proportionality factor between the applied field stress and the local tensile stress concentration around the microcracks, which takes the following simple form [32,41]:

$$f(a_k) = \begin{cases} \omega \cdot (b/a_k) & (a_k \leqslant b) \\ \omega & (a_k > b) \end{cases} \tag{3}$$

where ω is a material constant controlling the damage surface and b denotes the critical microcrack length which defines the failure of the REVs. These two constants can be determined from the slope of the failure curve of rock under triaxial compression [41].

For any stress state, the actual average length of the kth microcrack family, a_k, in the direction $\mathbf{n}_k$ may be determined from Eq. (2b). More specifically, when the local traction σ_t on the microcrack is positive (tension) and sufficiently large then K_{I} will approach the fracture toughness K_{IC}, and microcrack growth will take place. The early growth of microcracks will be stable since the interaction between them is small. That is why the local traction σ_t is assumed to be reduced with microcrack growth (see Eq. (3)) [34]. Accordingly, the microcrack will grow to some distance to reach an equilibrium point where $K_{\mathrm{I}} = K_{\mathrm{IC}}$. As the applied loads are increased, the microcrack will grow again to a new equilibrium state. When the microcrack length a_k increases to the critical length b, the separation distance between adjacent microcracks in the kth family becomes small enough that the effect of microcrack interaction becomes stronger and unstable crack growth occurs. This results in the gradual coalescence of microcracks to form large-scale fractures. For simplicity, it is assumed that the macroscopic fracture is formed instantaneously (brittle failure), and hence the condition $a_k = b$ can be defined as a criterion for the failure of the REV [26,28]. However, it should be noted that the failure, as defined by the above criterion,

is the point where the microcrack interaction begins (onset of the macroscopic fracture). In general, this will be somewhat before the point at which the final failure of the REV occurs by the full coalescence of microcracks. Therefore, such an assumption would make the microcracks more prone to coalesce and bifurcate to form the discrete macroscopic fractures.

2.2.2. Damage constitutive equations for poroelasticity

After defining the damage tensor and its evolution law, the poroelastic properties of the damaged rock material need to be defined. It is assumed that the REV of the rock is isotropic in the initial, undamaged state. To satisfy this assumption, the microcracks are assumed to be inserted uniformly and symmetrically within the REV. That is, all microcracks within the REV are uniformly classified into several families in each of which the microcracks have the same orientation, and the initial length and number density of the microcracks are the same for all families. But as damage accumulates due to microcracking in the REV, the element gradually evolves to anisotropy. Accordingly, the generalized anisotropic Biot theory [38] is assumed to be applicable for any stationary state of damaged saturated rocks [37], and thus the following state laws are deduced:

$$\begin{cases} \boldsymbol{\sigma} = \mathbf{C}(\mathbf{D}) : \boldsymbol{\varepsilon} - \boldsymbol{\alpha}(\mathbf{D}) p \\ p = M(\mathbf{D}) \cdot [\zeta - \boldsymbol{\alpha}(\mathbf{D}) : \boldsymbol{\varepsilon}] \end{cases} \tag{4}$$

where $\mathbf{C}(\mathbf{D})$ is the fourth rank elastic modulus tensor of damaged rock material which exhibits the classic Voigt symmetries $M_{ijkl} = M_{jikl} = M_{ijlk} = M_{klij}$, $\boldsymbol{\alpha}(\mathbf{D})$ denotes the symmetric ($\alpha_{ij} = \alpha_{ji}$) second rank anisotropic Biot effective stress coefficients tensor, scalar $M(\mathbf{D})$ is Biot modulus and ζ represents the change of fluid content per unit volume of porous skeleton.

The variation of elastic properties as well as the poroelastic parameters is a function of damage growth, which has been derived explicitly from thermodynamic potential and micromechanical analyses [29,38], as follows:

$$\begin{cases} C_{ijkl}(\mathbf{D}) = \lambda\delta_{ij}\delta_{kl} + \mu(\delta_{ik}\delta_{jl} + \delta_{jk}\delta_{il}) + A(\delta_{ij}D_{kl} + D_{ij}\delta_{kl}) \\ \quad + B(\delta_{ik}D_{jl} + \delta_{il}D_{jk} + D_{ik}\delta_{jl} + D_{il}\delta_{jk}) \\ \alpha_{ij}(\mathbf{D}) = \delta_{ij} - \frac{1}{3}\cdot\frac{C_{ijkk}(\mathbf{D})}{K_s} \\ M(\mathbf{D}) = \dfrac{K_s}{\left(1-\frac{1}{9}\frac{C_{iijj}(\mathbf{D})}{K_s}\right) - \phi\left(1-\frac{K_s}{K_f}\right)} \end{cases} \tag{5}$$

where λ and μ are Lame elastic constants of the initial undamaged material, A and B are two constants defining the damage-induced modification of the strain energy, K_s and K_f are the bulk modulus of solid constituent of rock material and fluid bulk modulus, respectively, and ϕ is the porosity. For completeness, the expansions of Eq. (5) for the 2-D problem are given in Appendix A.

2.2.3. Damage-induced permeability changes

In order to form a complete system for solving the coupled hydro-mechanical problem, it is necessary to introduce another governing equation, i.e. the fluid transport equation, to describe fluid flow in the permeable rock medium. Enforcing fluid mass conservation and Darcy's law, the transport equation for an incompressible fluid can be written as:

$$-\nabla\cdot\left(-\frac{\mathbf{K}(\mathbf{D})}{\upsilon}\cdot\nabla p\right) = \frac{\partial\zeta}{\partial t} = \frac{1}{M(\mathbf{D})}\frac{\partial p}{\partial t} + \frac{\partial}{\partial t}(\boldsymbol{\alpha}(\mathbf{D}) : \boldsymbol{\varepsilon}) \tag{6}$$

where $\mathbf{K}(\mathbf{D})$ is the overall permeability tensor of the REV and υ is the dynamic viscosity of the fluid. The permeability of brittle rocks can significantly increase with the propagation of microcracks. From the viewpoint of homogenization, the REV of the rock material, composed of a porous matrix and a random distribution of microcracks, can be treated as an equivalent homogenized porous medium with an overall permeability tensor. Such an overall permeability tensor $\mathbf{K}(\mathbf{D})$ can be decomposed into two parts: (i) the initial permeability tensor $\mathbf{K}_0$ due to initial porosity which represents flow in the micropores in the matrix of the REV and (ii) the microcracking-induced permeability tensor $\mathbf{K}_c(\mathbf{D})$. The total overall permeability tensor is hence $\mathbf{K} = \mathbf{K}_0 + \mathbf{K}_c(\mathbf{D})$. The permeability tensor for the porous matrix of the REV $\mathbf{K}_0$ is assumed to remain unchanged during the loading (i.e. the influence of effective stresses on the micropore deformation is neglected), but the crack permeability tensor $\mathbf{K}_c(\mathbf{D})$ depends on the length, orientation, average aperture and number density of microcracks in the REV. Shao [30] explored the variation of crack permeability with the evolution of damage using a micro–macro averaging procedure. This relation for the overall crack permeability tensor is followed here and for the 2-D plane problem it can be rewritten as:

$$\mathbf{K}_\mathbf{c}(\mathbf{D}) = \frac{1}{6}\sum_{k=1}^{N} m_k a_k R(a_k) e(\sigma_t', a_k)^3 (\boldsymbol{\delta} - \mathbf{n}_k \otimes \mathbf{n}_k) \tag{7}$$

where $R(a_k)$ is the connectivity coefficient, denoted by $\mathbf{R}(a_k) = t_1[(a_k - a_0)/(b - a_k)]^{t_2}$, t_1 and t_2 are constants reflecting the connectivity characteristics, $e(\sigma_t', a_k)$ is the average aperture of microcracks defined as $e(\sigma_t', a_k) = \pi a_k \sigma_t / E_0'$ where E_0 is the elastic modulus of the undamaged material and σ_t' is the local tensile stress acting on the microcrack, denoted as $\sigma_t' = \sigma_n + p + f(a_k)\mathbf{n}_k \cdot \mathbf{S} \cdot \mathbf{n}_k$.

2.3. Failure criterion and post-failure decay

The REV fails when the microcrack length in a certain orientation in the REV is equal to or greater than the critical microcrack length (b). The failure of the REV implies that it has entered into the post-failure regime where the stress–strain curve has peaked followed by a rapid stress drop and then a substantially unchanged residual strength. During the post-failure regime, the macroscopic behavior of the REV is dominated mainly by the unstable microcracking and the frictional sliding of the broken microcrack interface [42]. Few models have succeeded in quantitatively modeling the behavior in the post-failure regime from first principles and based on microscopic characteristics of the medium [34]. For simplicity, an isotropic softening model for post-peak behavior is adopted [35] while other more realistic schemes to follow post-peak softening are investigated.

It is assumed that the elastic modulus of a failed microscopic element degrades monotonically as a scalar damage variable [35], as follows:

$$E = (1 - D)E_0 \tag{8}$$

where E_0 is the initial elastic modulus of undamaged rock material and D is a scalar damage variable which is a function of the equivalent principal strain:

$$D = \begin{cases} 1 - \eta\varepsilon_{c0}/\varepsilon_c & (\varepsilon_{c0} \geqslant \varepsilon_c, \text{for compressive}) \\ 1 - \eta\varepsilon_{t0}/\varepsilon_t & (\varepsilon_{t0} \leqslant \varepsilon_t < \varepsilon_{tu}, \text{for tensile}) \\ 1 & (\varepsilon_{tu} < \varepsilon_t, \text{for tensile}) \end{cases} \tag{9}$$

with $\varepsilon_t = \sqrt{\sum_1^3 (\frac{|\varepsilon_i| + \varepsilon_i}{2})^2}$ for a tensile state (at least one of the principal stresses is tensile) and $\varepsilon_c = \min(\varepsilon_i)$ for a compressive state (all three principal stresses are compressive). Note that tension is taken to be positive in this paper.

In the above equations, ε_i are the principal strains which are positive in the case of tensile strains, ε_t and ε_c are the equivalent principal tensile and compressive strains, ε_{t0} and ε_{c0} are the equivalent principal tensile and compressive strains at the peak stress state (i.e. only just failed state), η denotes the residual strength coefficient which is equal to the ratio of peak strength to residual strength of rock, and ε_{tu} is the ultimate tensile strain which is defined by $\varepsilon_{tu} = \varsigma\varpi\varepsilon_{t0}$, where ς is defined as the ultimate strain coefficient.

According to Eqs. (8) and (9), the stiffness of the failed REV is isotropically reduced with the increasing equivalent principal strain. If the tensile equivalent principal strain exceeds the ultimate tensile strain, the REV is considered to be fully ruptured and a small magnitude of stiffness is assigned to it. This approach is similar to the smeared crack model, which greatly simplifies the simulation of initiation and propagation of macroscopic fractures.

2.4. Assignment of initial damage/heterogeneity

Brittle rock generally contains numerous pre-existing defects, i.e. initial damage. Such initial damage leads to the virgin mechanical and hydraulic properties varying randomly from point to point and with direction in the material, i.e. heterogeneity. Accommodating such heterogeneity is vital for modeling localized failure.

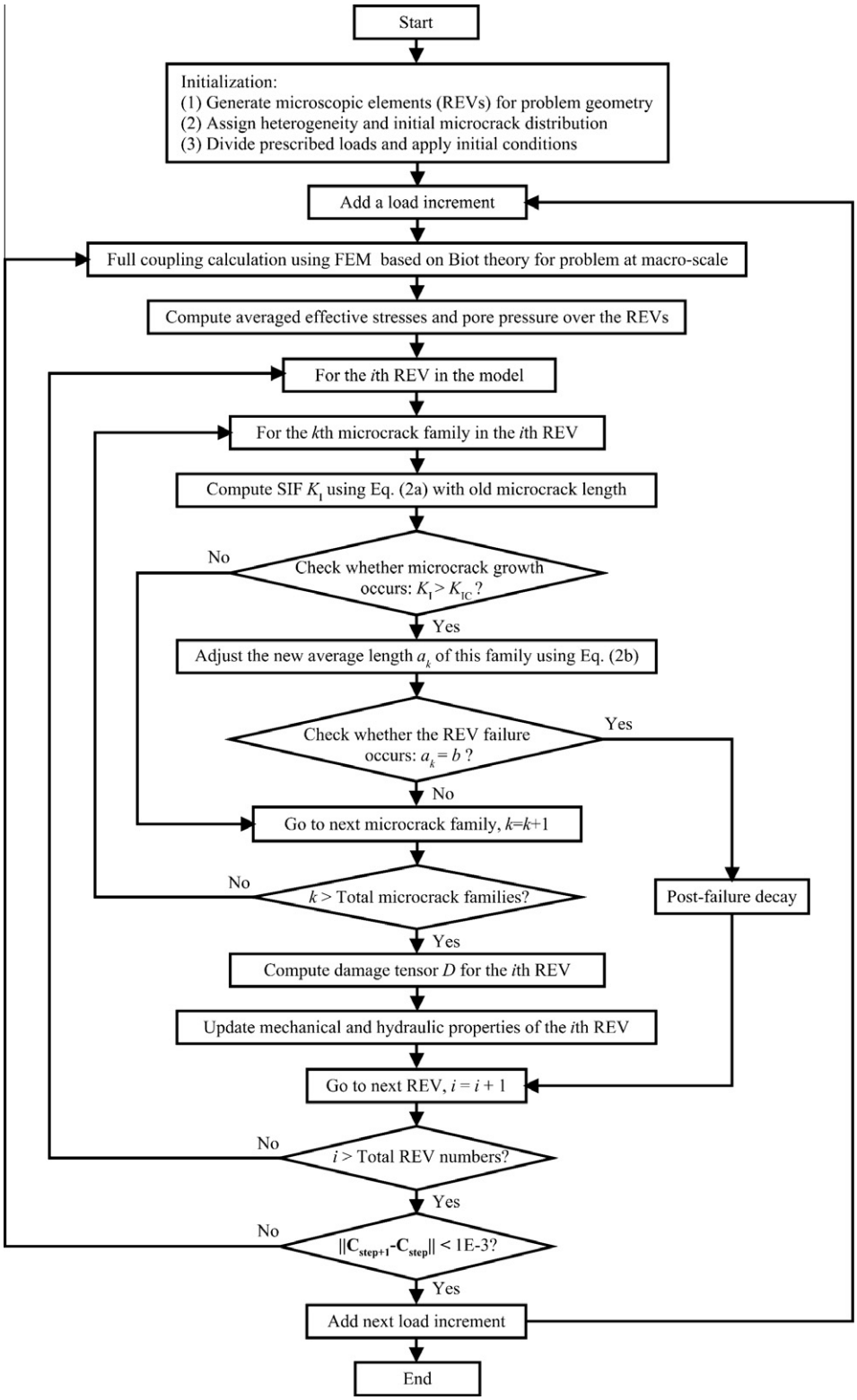

Fig. 2. Procedures for the implementation of coupled damage-flow modeling.

Two alternative approaches have been developed to represent realistic heterogeneity in rock. One is the statistical approach [35] which reconstructs heterogeneous properties at the microscopic level and the alternative is the deterministic approach where digital image processing techniques [43] are used to recover the material microstructure from the digital images recovered by X-ray CT scanning, acoustic velocity imaging, or a variety of other non-destructive geophysical methods.

Here we follow the statistical approach to randomly assign the initial mechanical and hydraulic parameters for each of the REVs. For the mechanical heterogeneity, the widely used Weibull distribution is adopted, which takes the following probability density function:

$$f(\xi_m, \bar{\xi}_m, \lambda_m) = \frac{\lambda_m}{\bar{\xi}_m} \cdot \left(\frac{\xi_m}{\bar{\xi}_m}\right)^{\lambda_m - 1} \cdot \exp\left[-\left(\frac{\xi_m}{\bar{\xi}_m}\right)^{\lambda_m}\right] \tag{10}$$

where ξ_m is the characteristic mechanical parameters (e.g. elastic modulus) for the REV, $\bar{\xi}_m$ is the scale parameter related to the average value of the characteristic parameters and λ_m defines the shape of the distribution function. For hydraulic heterogeneity a log-normal distribution function may be used to describe the permeability distribution [21] that is uncorrelated with the mechanical properties as:

$$f(\xi_h, \bar{\xi}_h, \lambda_h) = \frac{1}{\xi_h \lambda_h \sqrt{2\pi}} \cdot \exp\left[-\frac{\ln(\xi_h - \bar{\xi}_h)^2}{2\lambda_h^2}\right] \tag{11}$$

where ξ_h is the characteristic hydraulic parameter (e.g. permeability) for the REV, $\bar{\xi}_h$ and λ_h are the mean value of characteristic hydraulic parameter and its standard deviation, respectively. It is found that the shape parameters λ_m and λ_h can reflect the degree of material homogeneity. To be specific, the larger the values of λ_m and the smaller the values of λ_h the more homogeneous the resulting distribution of material properties [18,21,35]. According to Eqs. (10) and (11), multiple Monte-Carlo simulations can be utilized to generate heterogeneous distributions of material properties for each of the REVs.

2.5. Model implementation

This coupled damage and flow approach, based on the prior two-scale conceptual model is implemented as a continuum numerical method. This may be implemented in any continuum numerical model that accommodates Biot poroelasticity and that determines the solution of the fully coupled deformation and pore pressure fields – in our approach a finite element model is used. Additionally, this approach requires that the damage state and the damage-induced alteration of stiffness, poroelastic coefficients and permeability are continually updated with the increase in loads. Fig. 2 presents a flow chart for this coupled modeling approach. The basic procedures are summarized as follows:

(i) After the problem geometry has been defined, the model is discretized into a set of microscopic elements (REVs). Then multiple Monte-Carlo simulations are utilized to generate the initial mechanical and hydraulic properties and the microcrack distribution. The prescribed stress or displacement on the boundaries is divided into a series of discrete load increments. The incremental load is applied to the model gradually so as to ensure a quasi-static response.
(ii) For each loading increment, a fully coupled analysis is performed by FEM based on Biot theory, and the average effective stresses and pore pressure for each of the REVs are calculated.
(iii) Effective stresses and pore pressures defined over the REV are used in Eqs. (2a) and (2b) to determine the growth in length for the microcracks in all families. Then the damage tensor is calculated using Eq. (1). Furthermore, the tensors for the elastic modulus, Biot effective stress, Biot modulus and the overall permeability are modified following Eqs. (5) and (7), respectively. If the average microcrack length in any family in the REV exceeds the critical microcrack length (b), the REV is presumed to have failed and its stiffness is degraded isotropically using Eqs. (8) and (9).
(iv) The continuum finite element model with the updated material parameters is used to define a new equilibrium and steps (ii) and (iii) are repeated to examine the damage state. The next load increment is added only if the following convergence condition is satisfied: $\|\mathbf{C}_{step+1} - \mathbf{C}_{step}\|_\infty \leqslant 1 \times 10^{-3}$, where $\mathbf{C}$ is the elastic stiffness matrix.

The above procedures have been implemented in MATLAB to define the damaged constitutive parameters and implemented into the finite element model COMSOL Multiphysics to define spatial behavior.

3. Model validations

Two verification examples are followed to examine the implementation of the coupled damage and flow model. A first example explores the response of a single REV under simple loading condition to demonstrate the basic nature of the model. The second example follows the response of a biaxial compression experiment in the laboratory where the spatial evolution of damage and flow is followed together with the resulting nonlinear response to failure.

3.1. Elementary REV

The plane strain mechanical and steady-state hydraulic response is followed on a single REV with dimensions of 1 mm × 1 mm (Fig. 3). It is assumed that twelve ($N = 12$) sets of microcracks are inserted uniformly in the REV. The orientation angle of the ith microcrack is $\beta_i = \pi(i-1)/N$. The initial microcrack length and the number density of microcracks are assumed to be uniform in each orientation. The input model parameters used in the calculations [29,30,44] are summarized in Table 2. The sample is first loaded by an equal confining pressure and axial stress to establish an initial balance state. This is followed by an applied incremental axial displacement of $\Delta u_y = 5 \times 10^{-4}$ mm per loading step imposed to the top of the sample. The sample is assumed to be completely saturated throughout the loading, with a specific initial pore pressure p_0 and with constant fluid pressures p_t and p_b applied to the top and basal boundaries and with zero flux from the sides. Lateral confining stresses of $\sigma_x = 0$, 10 and 20 MPa and fluid pressures of $p_t = p_b = p_0 = 0$, 5 and 10 MPa were variously applied to investigate the deformation and flow behavior of the REV before rupture.

3.1.1. Stress–strain response

Fig. 4 shows the relationships between axial stress, axial strain and lateral strain for the REV before failure at different confining pressures and pore pressures. The model adequately replicates the anticipated non-linear strain hardening behavior with associated volumetric dilatancy in the pre-peak stress regime. As the confining stress increases, the ultimate strength also increases and the strain hardening range (inelastic behavior) widens. Increasing pore pressure illustrates the opposite tendency. The reason for this phenomenon is that the confining pressure suppresses the opening of microcracks and restrains their propagation while the fluid pressure accelerates microcrack growth.

Table 1
Notation.

Symbol	Description	Units
a_0	Initial microcrack length	m
a_k	Average microcrack length of the kth family	m
b	Critical microcrack length	m
e	Average aperture of microcrack	m
m_k	Microcrack number density of the kth family	m^{-3}
$p, \bar{p}$	Pore pressure and average pore pressure	Pa
t_1, t_2	Connectivity coefficients	–
A, B	Damage influence coefficients	Pa m^3
C	Borehole pressurization rate	Pa/s
D	Scalar damage variable	–
E_0, υ_0, λ, μ	Initial elastic modulus, Poisson's ratio, Lame constants	Pa, –, Pa, Pa
ΔP, Δt	Pressure increment and time increment	Pa, s
P_i, P_b	Fracture initiation pressure and breakdown pressure	Pa
R	Connectivity coefficient	–
K_s, K_f	Solid constituent bulk modulus and fluid bulk modulus	Pa
K_{IC}	Mode I fracture toughness	Pa $m^{1/2}$
N	Total families of microcracks in the REV	–
M	Biot modulus	Pa
α	Scalar Biot effective stress coefficient	–
β	Microcrack orientation angle	–
$\varepsilon_t, \varepsilon_c, \varepsilon_{t0}, \varepsilon_{c0}$	Equivalent tensile and compressive strains	–
ε_{tu}	Ultimate tensile strain	–
ϕ	Porosity	–
σ'_t	Local tensile stress on microcrack	Pa
ω	Damage surface coefficient	–
ζ	Fluid content change	–
ς	Ultimate strain coefficient	–
λ_m, λ_h	Mechanical and hydraulic homogeneity indices	–
υ	Fluid dynamic viscosity	Pa s
η	Residual strength coefficient	–
$\mathbf{n}_k$	Unit normal vector of microcrack in the kth family	–
$\boldsymbol{\alpha}$	Biot effective stress coefficients tensor	–
$\boldsymbol{\sigma}$, $\bar{\boldsymbol{\sigma}}'$	Total stress tensor and effective stress tensor	Pa
$\mathbf{D}$	Damage tensor	m^{-3}
$\mathbf{K}$, $\mathbf{K}_0$, $\mathbf{K}_c$	Permeability tensor	m^2
$\mathbf{S}$	Deviatoric stress tensor	Pa
$\mathbf{C}$	Elastic modulus tensor	Pa

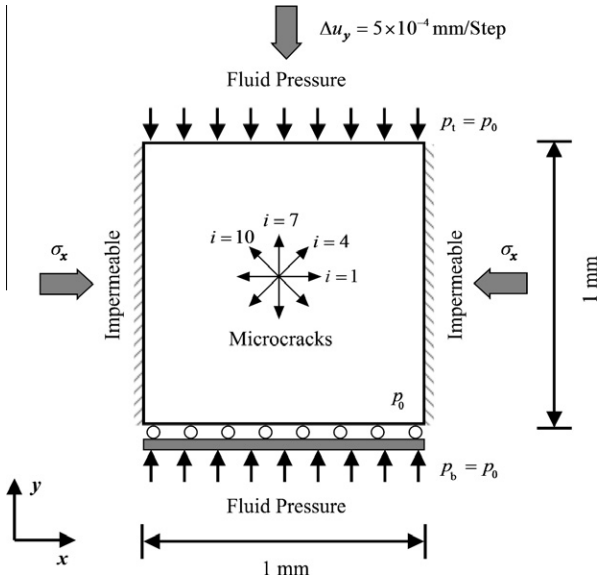

Fig. 3. Model geometry and loading conditions for the single element REV test. The microcracks are assumed to be inserted uniformly in the REV. Δu_y is the applied incremental axial displacement, σ_x is the confining stress and p_0, p_t and p_b are the fluid pressures.

Table 2
Model parameters used in the single element REV test.

Identity	Values
Mechanical properties	Initial elastic modulus and Poisson's ratio: E_0 = 10 GPa, υ_0 = 0.25 Mode I fracture toughness of microcrack: K_{IC} = 1.1 MPa $m^{1/2}$ Damage influence coefficients: A = 200 Pa m^3 B = − 800 Pa m^3 Bulk modulus of rock grain constituent: K_s = 40 GPa
Microcrack parameters	Initial microcrack length: a_0 = 0.1 mm Critical microcrack length: b = 0.3 mm Microcrack number density: m = 0.23 mm^{-3} Damage surface coefficient: ω = 0.60
Hydraulic properties	Bulk modulus of fluid: K_f = 3.3 GPa Dynamic viscosity of fluid: $\upsilon = 1\times10^{-3}$ Pa s Initial permeability: $k_0 = 1.0\times10^{-17}$ m^2 Porosity: φ = 5% Connectivity coefficients: t_1 = 100, t_2 = 1.0

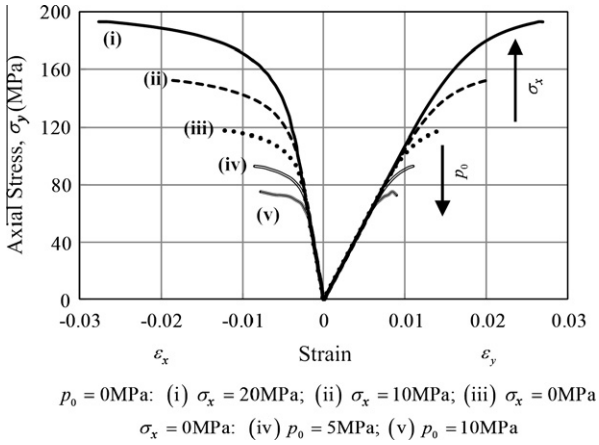

Fig. 4. Relationships between axial stress (σ_y), axial strain (ε_y) and lateral strain (ε_x) obtained from the elementary simulations at different confining pressures and pore pressures (σ_x, p_0).

3.1.2. Damage growth and induced permeability change

The accumulation of damage together with the evolution of permeability for this elemental REV test is displayed in Fig. 5. The two components of damage tensor and that of permeability tensor are shown in Fig. 5a for the x- and y-coordinate directions, respectively. Damage is accumulated mainly in the x-direction while the major change in permeability is, as expected in the orthogonal (y-) direction. This results from the microcracks primarily growing parallel to the loading axis (i.e. y-direction). Moreover, the damage component D_{11} only begins to accumulate when the rock is stressed over 50% of the peak stress (ultimate strength) at which point it increases markedly. The permeability component k_{22} also alters in a similar way and its value at peak stress state is about 10^3 times that of the magnitude of the initial permeability.

Fig. 5b shows the variation of damage component D_{11} and permeability component k_{22} with an increase in axial stress at different confining pressures and pore pressures. As can be seen from the figure, the stress threshold for the onset of damage and permeability change depends on the effective confining pressure. The evolution rate of damage and permeability is faster as the effective confining pressure is reduced (confining pressure lower or pore pressure higher), that is to say, at the same level of axial stress the damage and permeability decrease with the increase of effective confining pressure. From a qualitative point of view, the general trend in damage growth and its influence on permeability

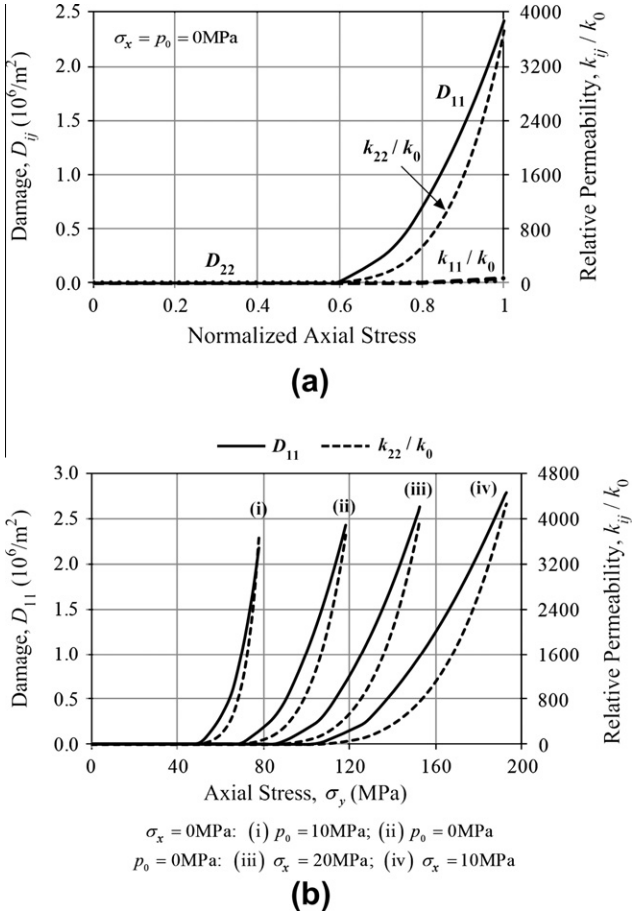

Fig. 5. Evolution of damage and permeability for the single element REV test: (a) two components (D_{11} and D_{22}) of the damage tensor and that (k_{11}/k_0 and k_{22}/k_0) of the permeability tensor as a function of normalized axial stress (axial stress/peak axial stress) at σ_x = 0 MPa and p_0 = 0 MPa; (b) variation of D_{11} and k_{22}/k_0 with axial stress at different confining pressures and pore pressures.

change produced by the model is in good agreement with many reported experimental [31,41,45] and numerical [46] observations.

Finally, it should be pointed out that the reduction of initial permeability during the elastic deformation stage which results from the closure effect of initial microcracks and micropores is not incorporated in the present model, but such changes in initial permeability are generally smaller than the magnitude of permeability induced by damage growth [45] and its effect can generally be ignored.

3.1.3. Damaged poroelastic properties

The variation of elastic modulus and Biot effective stress coefficients of the damaged REV with the normalized axial stress are shown in Fig. 6, where E_0 and G_0 are the initial elastic modulus and shear modulus of rock, respectively. It is observed that the axial modulus (C_{22}) remains near constant while the lateral modulus (C_{11}) and shear modulus (C_{12}) deteriorate significantly with the increasing axial stress. This can be explained by the fact that most of the induced damage is accumulated in the lateral direction (x-coordinate direction). Correspondingly, the Biot effective stress coefficient in the axial direction (α_{22}) is only affected slightly by this induced damage but that in lateral direction (α_{11}) increases by ~6%. These features of anisotropic poroelastic behaviors reproduced by the model are qualitatively consistent with experimental observations [25,29,37].

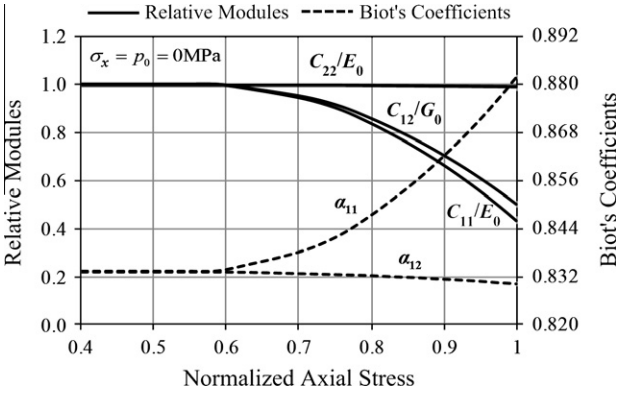

Fig. 6. Variation of relative modulus (C_{11}/E_0, C_{22}/E_0 and C_{12}/G_0) and Biot effective stress coefficients (α_{11} and α_{22}) with the normalized axial stress in the elementary test at σ_x = 0 MPa and p_0 = 0 MPa. E_0 and G_0 are the initial elastic modulus and shear modulus.

3.2. Biaxial loading in compression

The progress of standard compression experiments is followed using the coupled damage and flow model to verify the general representative behaviors of the model including the complete load-deformation history, permeability evolution and failure modes via a qualitative comparison with available experimental results. The geometry of the numerical experiments is shown schematically in Fig. 7. The sample is a rectangular domain with dimensions of 50 mm × 100 mm and is discretized into 50 × 100 = 5000 REVs, in each of which it is assumed that twelve (N = 12) groups of microcracks were inserted with the parameters given in Table 2. In addition, the effects of initial damage on the mechanical and hydraulic properties, particularly the elastic modulus and permeability, were incorporated by randomly assigning these parameters in a Weibull distribution defined by Eq. (10) and in a log-normal

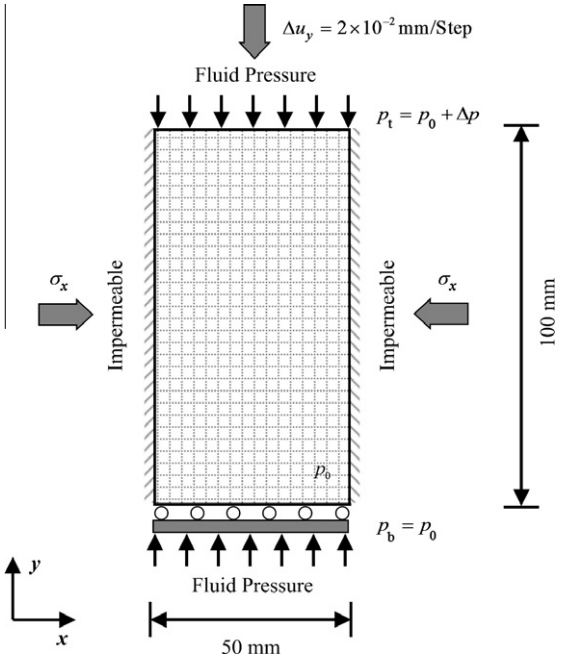

Fig. 7. Model geometry and loading conditions for the standard biaxial compression experiment. The model is meshed by 50 × 100 = 5000 REVs. Δu_y is the applied incremental axial displacement, σ_x is the confining stress, p_0 is the initial pore pressure and Δp is the differential pressure between the upstream fluid and the downstream fluid.

Table 3
Model parameters used in the biaxial experiment simulation.

Parameter names	Values
Overall elastic modulus, $\bar{\xi}_m$	10 GPa
Homogeneity index of elastic modulus, λ_m	1.5, 2.5, 3.5 and 5.0
Overall permeability, $\bar{\xi}_h$	1×10^{-17} m^2
Homogeneity index of permeability, λ_h	1.0,1.5, 2.0 and 2.5
Residual strength coefficient, η	0.1
Ultimate tensile strain coefficient, ς	5

distribution defined by Eq. (11). These distributions were ascribed to each of the REVs to model the localized failure and flow in the sample. All mechanical, hydraulic and post-failure decay parameters are as listed in Table 3.

Congruent with the procedure adopted by typical triaxial compression experiment [47] (that actually apply a biaxial stress state), a constant confining pressure σ_x in combination with the axial stress was applied equally to achieve an initial hydrostatic stress state. Subsequently, an incremental axial displacement of $\Delta u_y = 2 \times 10^{-2}$ mm per loading step was applied to the top of the sample until its load-bearing capacity was completely lost. The simulations were run with the scheme of steady-state fluid flow, in which the upstream fluid pressure p_t and downstream fluid pressure p_b were kept unchanged and a constant differential pressure of $\Delta p = p_t - p_b = 0.1$ MPa between them was maintained throughout the test.

With the aim of reproducing the macroscopic hydraulic and mechanical behaviors during the failure process, several macroscopic variables are needed to describe the modeling results. These are stress, engineering strain, overall permeability and acoustic emission event rates and energy release. Stress–strain curves are derived from the simulation results by conversion of boundary forces and displacements. The overall permeability of the sample is derived based on Darcy's law, as follows [20]:

$$K = \frac{H}{\Delta p} \cdot Q = \frac{H}{p_t - p_b} \cdot \sum q \tag{12}$$

where $Q = \sum q$ is the total flux flowing through the sample, $\Delta p = p_t - p_b$ is the differential fluid pressure between the top and the bottom of the sample and H is the length of the sample.

Acoustic emission (AE) is defined as transient elastic waves within the material, caused by the release of elastic energy due to microcracking in stressed material. It offers useful information for indirectly identifying the evolution of damage within rock [48]. An approximate approach for calculating AE events and energy release is used [17] in which it is assumed that each AE event corresponds to the damage of an element and that the strain energy released by damaged elements is all in the form of radiated seismic energy (acoustic emissions). We follow this approach here to account for the number of the damaged REVs in the numerical model as the AE event counts and then calculate the reduced elastic strain energy of the REVs due to damage as the AE energy is released.

3.2.1. Biaxial load behavior

The first sets of simulations are performed on samples with a homogeneity index of elastic modulus of $\lambda_m = 2.5$ and an initially homogeneous permeability. A lateral confining stress of $\sigma_x = 5.0$ MPa and an initial pore pressure of $p_0 = 1.0$ MPa are applied to the sample before the incrementing of axial displacement to provide the loading.

Fig. 8 shows the resulting axial stress, overall axial permeability and AE event counts as a function of axial strain during the failure process of the sample under biaxial compression. In the figure, the overall axial permeability is calculated by Eq. (12). In general, the

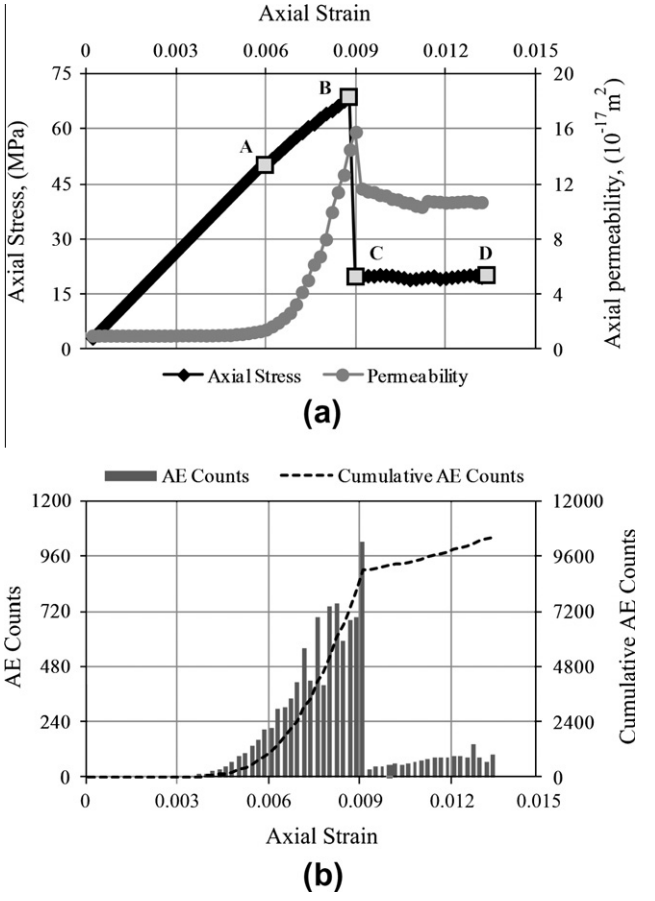

Fig. 8. Biaxial compression simulation results of (a) axial stress and overall axial permeability versus axial strain, and (b) AE event counts and cumulative AE event counts occurring over specified axial strain interval.

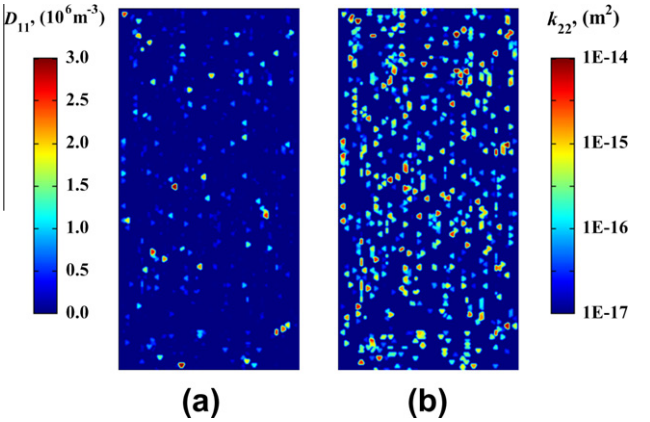

Fig. 9. Random distribution of (a) x-direction damage and (b) y-direction permeability at the load level labeled by Point A on the stress–strain curve in Fig. 8a.

numerically-obtained evolution of deformation of the sample, as evident in the complete stress–strain curve and the overall axial permeability curve, can be characterized into four stages: a linear elastic stage (OA), a nonlinear hardening stage (AB), a stage containing a sudden stress drop (BC) and an asymptote to residual strength (CD). In each of the four stages, the macroscopic feature of deformation, permeability and AE activities are closely related to the microscopic damage evolution with the sample.

In the linear elastic stage (OA in Fig. 8a), the simulated overall axial permeability remains constant due to the small amount of

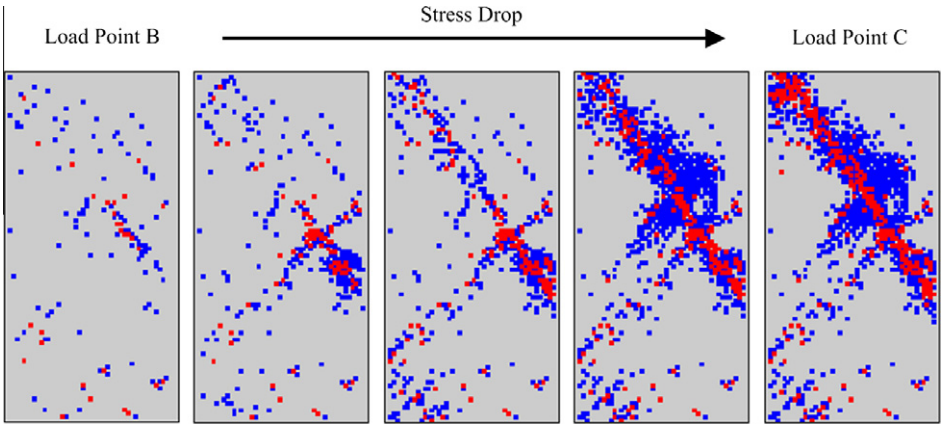

Fig. 10. Local microscopic elementary damage concentration into a macroscopic shear failure band during the sudden stress drop stage (i.e. Point B to C on the stress–strain curve in Fig. 8a). Different colors indicate the state of all the REVs: the gray for the unruptured REVs, the blue for the ruptured REVs but still maintaining residual strength and the red for the completely ruptured REVs. (For interpretation of the references to color in this figure legend, the reader is referred to the web version of this article.)

damage occurring. However, the reduction of permeability in this stage, observed in reported experiments (see for example, Ref. [47]), is not replicated by the present model. The reason for this is that the closure effect of microcracks and micropores under compression is not included in this model. As the load reaches ~70% of the peak stress (Point A in Fig. 8a), the elementary damage and permeability are distributed somewhat randomly throughout the sample (see Fig. 9). From Point A, the sample enters a stage of non-linear hardening. The simulated overall axial permeability increases sharply in this stage prior to the sample reaching peak stress as a result of the accelerated growth and coalescence of microcracks. Also, the numerically-obtained AE event counts, reflecting the evolution of damage due to microcracking within the sample, increase smoothly and continuously with the increase in load before the peak stress (OB in Fig. 8b).

The numerically-obtained macroscopic fracture pattern becomes evident just after the peak stress (Point B in Fig. 8a), accompanied by a dramatic loss in load-bearing capacity. The sequential diagrams in Fig. 10 clearly illustrate during the unloading portion of stress–strain curve (Points B–C in Fig. 8a) how the local damaged REVs continue to propagate and coalesce and eventually self-organize into a macroscopic shear fracture inclined at an angle to the loading direction. In these figures the state of all the REVs are denoted with different colors: the gray background for those unruptured REVs, the blue dots for the failed REVs that still retain residual strength (i.e. partially ruptured REVs) and the red dots for the failed REVs which have completely lost their load bearing capacity (i.e. fully ruptured REVs). It is interesting to observe that the macroscopic shear fracture, comprising the fully ruptured REVs clustered in the center of the partially ruptured zones, are well reproduced by the present numerical model in which only the Mode I fracture criterion is employed, rather than some shear-stress related strength criterion (e.g. Mohr–Coulomb criterion). Such observation may confirm the most common interpretation of shear failure which holds that the macroscopic propagation of shear fracturing is caused by the linkage of many tensile microcracks [49].

Moreover, the simulated overall axial permeability reaches a maximum soon after the peak stress which is approximately 20 times that of the initial magnitude. The maximum overall permeability is much smaller than the local elementary permeability in the macroscopic fracture (about three orders of magnitude smaller than initial permeability), as shown in Fig. 11a. Such difference may be explained by the fact that the macroscopic flow behavior depends not only on the local elementary permeability but also on the connectivity of the more conductive elements. As can be

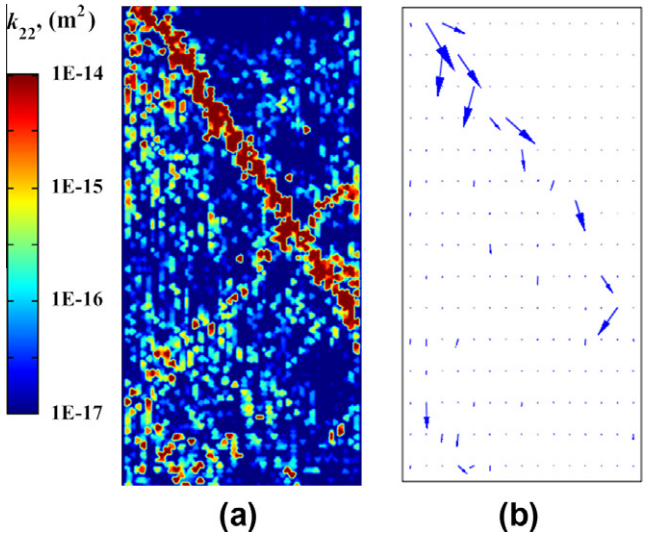

Fig. 11. Distribution of (a) *y*-direction permeability and (b) flow vector at the load level labeled by Point C on the stress–strain curve in Fig. 8a.

seen from Fig. 11a, the higher permeability only occurs in the inclined macroscopic shear fracture, outside of which other lower permeability zones act as barriers to fluid flow. As a result, the overall macroscopic permeability of the sample is not increased significantly. Such localized flow behavior is demonstrated more distinctly by[1] Fig. 11b in which the flow velocity vectors are represented by the blue arrows. It can be seen that the fluid flows preferentially and rapidly along the nucleated macroscopic fracture. The fractured zones provide the fast pathways for the migration of fluid while the unruptured zones block the fluid transport.

Finally, in the stage of residual deformation, the numerically-produced axial stress approaches an asymptote of residual strength and the AE event counts decrease to a low level (CD in Fig. 8). Also, it is observed that the simulated overall axial permeability is reduced by ~36% of that at the peak stress. This can be explained by the fact that the overall axial permeability of the numerical sample depends on not only the higher permeability zones in the macroscopic shear fractured band but also the lower permeability zones outside the band (see Fig. 11a). The elastic closure of micro-

[1] For interpretation of color in Fig. 11, the reader is referred to the web version of this article.

cracks in the lower permeability zones at residual strength, because of the decrease of local traction on the surface of microcracks, which further block the fluid flow in axial direction. However, it should be noted that such an effect of microcrack closure in the present model may be amplified due to neglecting the irreversible inelastic deformation of microcracks, which results in the substantial decrease in permeability. Actually, the permeability reduction in the residual period, reported in the laboratory experiment [47], is primarily controlled by the conjugate shear fracture that transects the sample and the resulting comminution along that feature [47,50].

Despite ignoring some mechanisms of microcrack deformation, it can be concluded that the present model provides a general two-scale approach for predicting the evolution process from microcracking to macroscopic fracturing and the associated behavior of fluid flow of brittle rocks under the coupled hydraulic-mechanical loading, subject to suitable calibration.

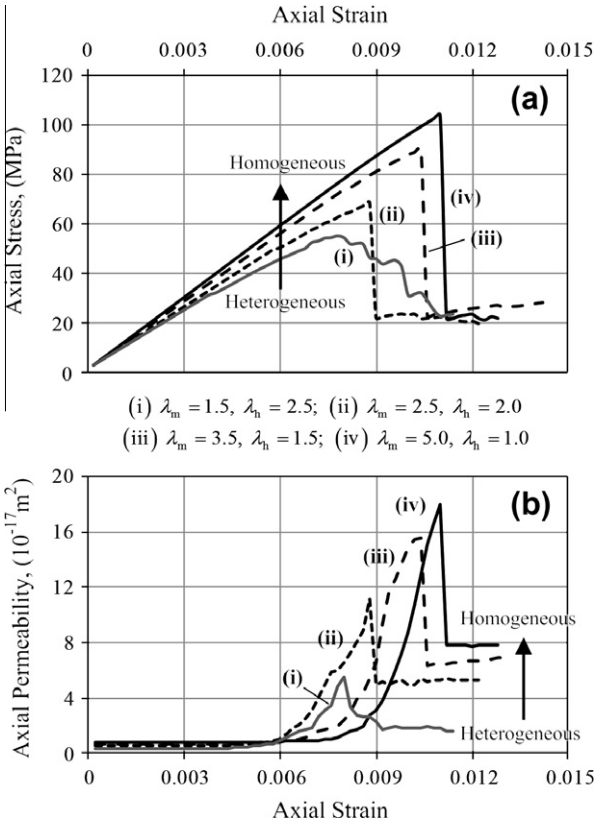

Fig. 12. Evolution of (a) axial stress and (b) overall axial permeability as a function of axial strain for four simulated samples with different degrees of heterogeneity.

3.2.2. Effect of heterogeneity

As noted above, rock is generally heterogeneous in both mechanical and hydraulic properties, which can be represented by the Weibull and lognormal distributions, respectively. This heterogeneity plays a vital role in determining the fracture patterns and flow paths in rock. To illustrate this point, simulations were performed under biaxial loading using four pairs of mechanical and hydraulic homogeneity indices (λ_m, λ_h), i.e. (1.5, 2.5), (2.5, 2.0), (3.5, 1.5) and (5.0, 1.0) (see Table 3). These specific values impart material property distributions ranging from highly heterogeneous to homogeneous, respectively.

The influence of heterogeneity on hydro-mechanical behavior of rock can be seen from the stress–strain curve, permeability response and fracture patterns. Fig. 12 depicts the evolution of axial stress and permeability as a function of axial strain for four simulated samples with varying degrees of heterogeneity. It is clear that the stress–strain relationship and the permeability evolution depend strongly on the heterogeneity of the sample. The samples with higher heterogeneity show more ductile post-failure behavior while those with higher homogeneity fail in a brittle manner. Moreover, increasing heterogeneity leads to both a reduced peak strength and with permeability augmentation occurring at smaller axial strain. The fracture patterns for each of the four degrees of heterogeneity are shown in Fig. 13. It is found that more ruptured REVs occur and distribute randomly within the highly heterogeneous samples but within the highly homogenous samples there are only a few failed REVs concentrated around the macroscopic fracture. This is thought to be a consequence of a ruptured REV leading to widespread failure of the adjacent REVs since they have similar strengths within homogeneous samples.

4. Numerical simulation of hydraulic fracturing

We now explore the roles of heterogeneity and damage on the progressive propagation of hydraulic fractures driven by pressurization of a borehole. Numerous theoretical models and numerical algorithms have been developed to predict the evolution of hydraulic fractures created by injecting a viscous fluid from a borehole (see Refs. [19,51–53] for detailed reviews). The development of the fracture following initiation from the borehole wall requires consideration of the propagation of damage and may be accommo-

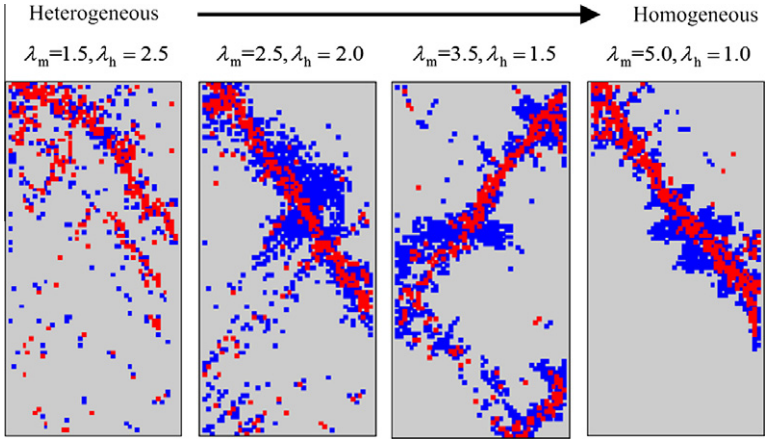

Fig. 13. Fracture patterns for four simulated samples with different degrees of heterogeneity.

dated by damage models as described previously – provided that compatibility between fluid flow and the evolution of damage is maintained. Such effects are essential to the modeling of the propagation of hydraulic fractures in a numerically efficient and physically realistic manner, particular in accurately predicting the critical pressures and fracturing paths [19,51]. Motivated by this, we here focus on the modeling of the evolution of fracturing driven by hydraulic pressure in permeable rocks from the viewpoint of coupled damage-flow interactions. Simulations are performed to show how the proposed model predicts the behavior of time-dependent pressurizing fluid penetrating into the ruptured wall of the borehole and the resulting induced fracturing away from the borehole. The effects on initiation pressure and breakdown pressure of heterogeneities, borehole pressurization rate and permeability are taken into account and comparisons of numerical results with available experimental data are discussed.

4.1. Model geometry

The 2D hydraulic fracture problem considered herein, is a cross-section through a vertical borehole drilled within a porous permeable rock which is assumed to be isotropic in the initial, undamaged state, subjected to an initial anisotropic stress field with maximum principal stress component σ_1 and minimum principal stress component σ_3. The initial pore pressure field in the rock is neglected and the pressurizing fluid is injected into the borehole at a constant pressurization rate C until unstable fracture propagation occurs. This problem can be analyzed by assuming the plane strain condition and transient state fluid flow. Taking advantage of the problem half symmetry, the problem geometry is a rectangular region of 200×100 mm with a half hole of $R_0 = 10$ mm radius located half-way along one-side of the mesh. The geometry comprises $200 \times 100 = 20{,}000$ microscopic elements (REVs), as shown in Fig. 14a. The boundary conditions correspond to a roller along the left side and the line of symmetry and tractions applied at the top boundary (σ_1) and the right boundary (σ_3). All boundaries are zero flux boundaries except for the borehole where the fluid is injected as an increasing hydraulic pressure P with time (P is represented by a step function, as shown in Fig. 14b). The relevant material parameters used in the simulations are shown in Tables 2 and 3.

4.2. Effective stress and pore pressure field around borehole

The first basic problem we are here interested in is the evolution of poroelastic stress around the borehole caused by fluid pressurization. Also, this problem provides a further validation test for the modeling of coupled hydraulic-mechanical processes. The closed-form poroelastic solutions for a borehole "instantaneously" drilled in a non-hydrostatic stress field [54] presents the short-time asymptotic solutions for the region near the borehole. Following these solutions, the stress field and pore pressure distribution around the pressurized borehole can be derived analogously.

Simulations which assume that no damage occurs in the rock were performed to define the poroelastic effects around the borehole. The maximum principal stress, σ_1, and minimum principal stress, σ_3 are -6.0 MPa and -1.0 MPa, respectively. A constant fluid pressure, P, of 1.0 MPa is applied in the borehole. A two-step solution scheme is utilized to simulate the realistic process of fluid injection whereby the numerical calculation is first performed in the mechanical-only model to reach an initial equilibrium, and then with this equilibrium state as initial conditions, the calculation is subsequently run in the solid–fluid coupling model to a specific time. The variation of pore pressure, tangential and radial effective stresses with radius are compared to the analytical results for three values of early times ($t = 0.01$ s, 0.05 s and 0.1 s) and along

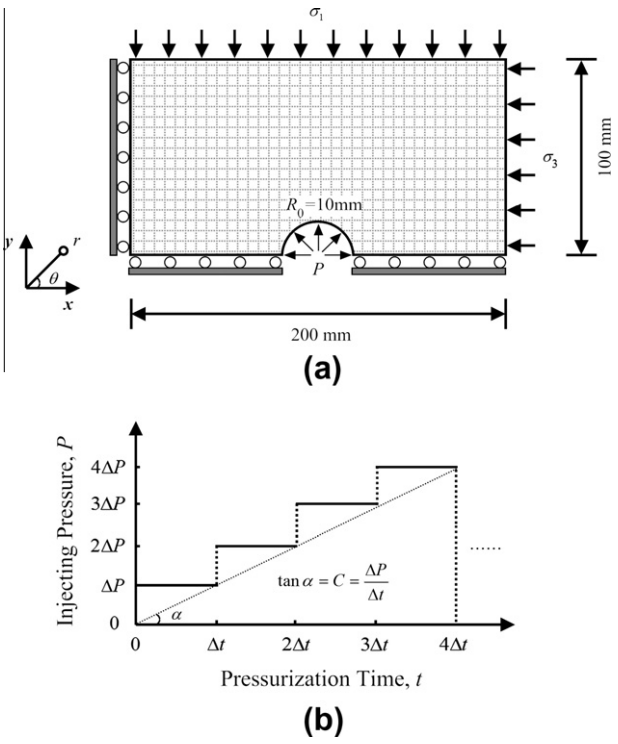

Fig. 14. Model setup for hydraulic fracturing at laboratory scale: (a) specimen geometry and loading conditions and (b) injecting pressure (P) versus pressurization time (t). σ_1 and σ_3 are the maximum and minimum principal stress components, respectively. The pressurization rate is defined as $C = \Delta P/\Delta t$, where ΔP and Δt are the increment of fluid pressure and time, respectively.

the direction of the vertical diameter ($\theta = 90°$) in Fig. 15. The figure shows clearly that the numerical simulation results agree well with the analytical predications. Moreover, it is noted that the pore pressure and effective stress on the borehole wall are independent of time, but they increase gradually with time in the vicinity of the borehole. On the borehole wall ($r = R_0$), the tangential effective stress is tensile and it reaches a maximum value of $\sigma'_\theta = 4.3$ MPa at the point $\theta = \pi/2$. This is congruent with the reduced form of these expressions for maximum tangential effective [55] as:

$$\sigma'_{\theta\max} = P[2 - \alpha(1 - 2\upsilon_0)/(1 - \upsilon_0)] + 3\sigma_3 - \sigma_1 = 4.4\ \text{MPa} \qquad (13)$$

where α is a scalar Biot effective stress coefficient and υ_0 is Poisson's ratio. This equation also indicates that the maximum tangential effective stress is determined by just the borehole pressure P and is independent of time and the pore pressure distribution beyond the borehole wall. This implies that the traditional hydraulic-fracturing criterion based on Eq. (13) cannot interpret the effect of permeability and pressurization rate on breakdown pressure [56].

4.3. Evolution of hydraulic fractures

In hydraulic fracturing, a critical problem of interest is how to appropriately predict the failure mode of rock under conditions of fluid injection and the associated breakdown pressure. To illustrate this point, numerical simulations are completed using this coupled damage-flow model to represent the progressive hydraulic fracturing process. The numerical specimens are assumed to have a homogeneity index of elastic modulus of $\lambda_m = 2.5$, a homogeneous permeability, and they are subjected to a maximum principal stress of -6.0 MPa and minimum principal stress of -1.0 MPa. The fluid is injected into the borehole at a constant pressurization rate of $C = \Delta P/\Delta t = 0.50$ MPa/s, where $\Delta P = 0.5$ MPa denotes the pressure increment and $\Delta t = 1.0$ s denotes the time increment.

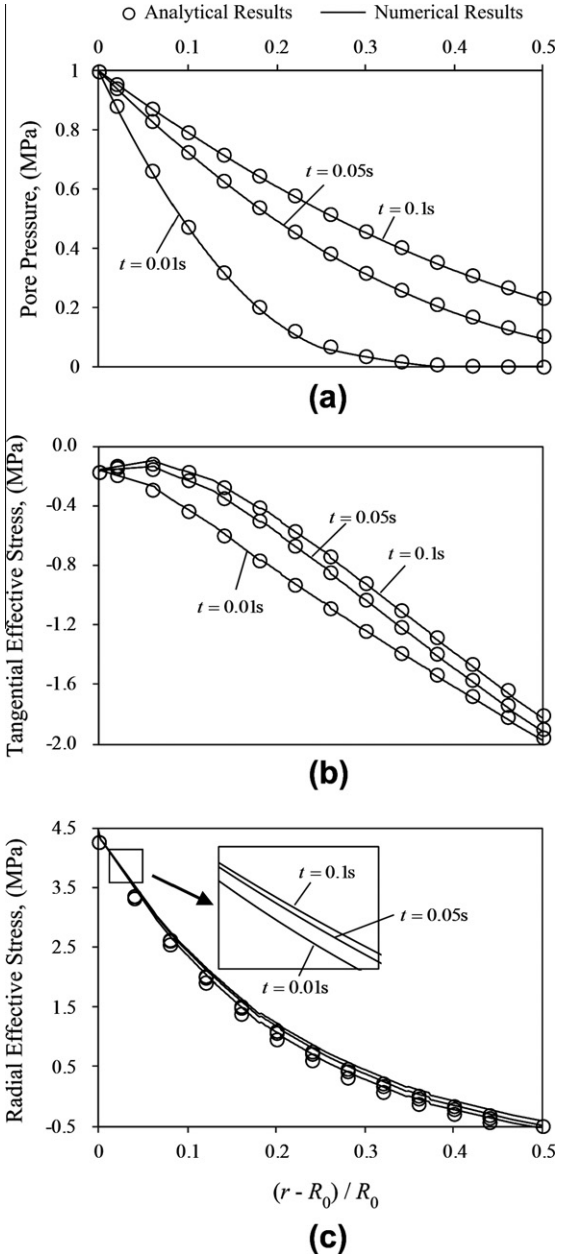

Fig. 15. Analytical and simulated poroelastic stress variations around the borehole with radius at $\theta = 90°$ for the specified time ($t = 0.01$ s, 0.05 s and 0.1 s): (a) pore pressure (p), (b) tangential effective stress (σ'_θ), and (c) radial effective stress (σ'_r).

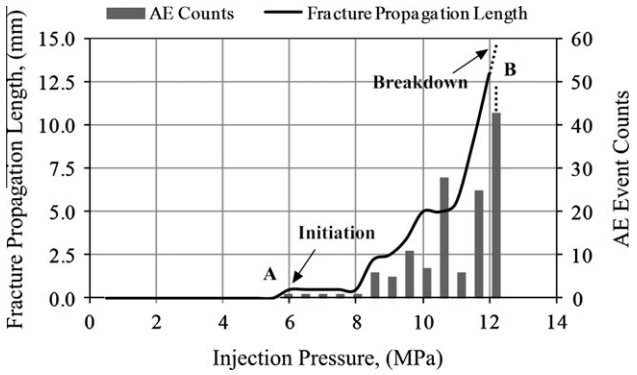

Fig. 16. Fracture propagation length and AE event counts as a function of injection pressure for the simulated specimen with a homogeneity index for the elastic modulus of $\lambda_m = 2.5$. The fluid is injected into the borehole at a constant pressurization rate of $C = 0.50$ MPa/s.

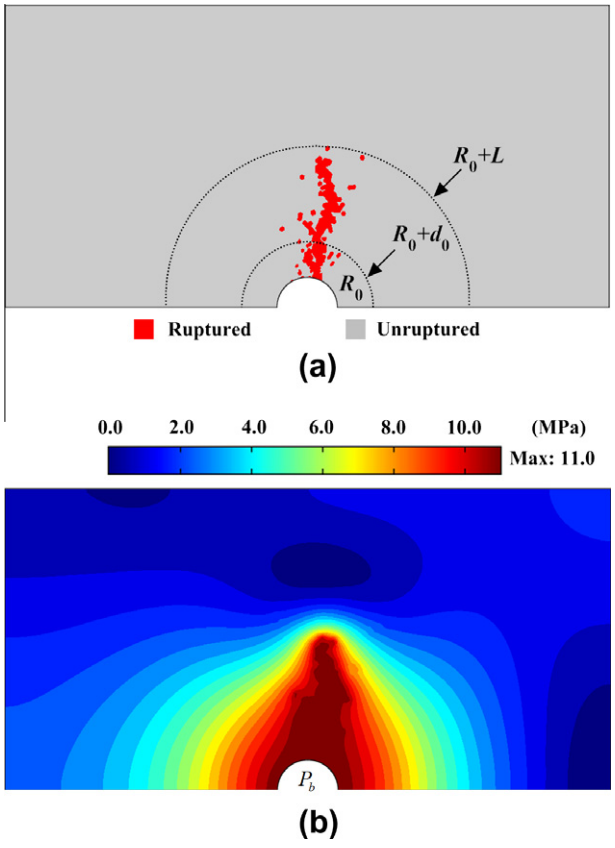

Fig. 17. Numerically obtained (a) hydraulic fracture patterns and (b) pore pressure distribution in the specimen with homogeneity index of elastic modulus of $\lambda_m = 2.5$ for a particular computation step under the breakdown pressure. L is defined as the hydraulic fracture propagation length, d_0 is a distance at which the unstable hydraulic fracture initiates at breakdown pressure, and R_0 is the radius of the borehole.

Fig. 16 presents the resulting fracture propagation length and AE event counts as a function of injection pressure during the borehole pressurization process. The fracture propagation length L is calculated by the radius of a circle which just covers the fractured zones, as shown in Fig. 17a. As can be seen from Fig. 16, there are two typically critical points (i.e. Points A and B) to distinguish the different stages of the hydraulic fracturing process. When the fluid pressure is increased to Point A ($P_i = 6.0$ MPa), acoustic emissions are activated immediately. This implies that the fracture first begins to propagate. Following Ref. [19], the pressure at Point A is called the fracture initiation pressure, P_i. Beyond Point A, the continually increasing fluid pressure drives the fracture to propagate stably until the pressure reaches Point B, where $P_b = 12.0$ MPa. At Point B, the acoustic emission event rate increases dramatically and the facture propagates without increasing the hydraulic pressure. The pressure at Point B is defined as the breakdown pressure, P_b. It is seen that the fracture initiation pressure P_i is about 50% of the corresponding breakdown pressure P_b. In addition, the unstable hydraulic fracture initiates under the breakdown pressure at a point apart from the borehole wall by a distance of $d_0 = 8.9$ mm (see Fig. 17a), rather than a point on the borehole wall predicted by the conventional theories of hydraulic fracturing [55,57]. These observations are also supported by recent theoretical and experimental investigations [58,59].

Furthermore, Fig. 17 displays the view of the hydraulic fracture patterns and the associated pore pressure distribution in the numerical specimen for a particular computation step under the breakdown pressure. From Fig. 17a, it is seen that the macroscopic hydraulic fracture grows progressively in the direction parallel to the maximum principal stress σ_1. However, the fracture shows a relatively rough and irregular trajectory. This is caused by the heterogeneity of the specimen. Indeed, the fracture propagation is controlled by the pre-existing field of defects (initial damage) in the material with statistical features. In addition, it is also interesting to note from Fig. 17b that a connected flow path is created which conducts fluid directly from the borehole to the open hydraulic fracture. That is why the pore pressure within the fracture is identical to the injection pressure in the borehole. Such fracture and flow patterns closely resemble the observations in hydraulic fracturing experiments [60]. It also confirms that the proposed numerical model is capable of capturing the evolution of fracturing and flow in a physically realistic manner.

4.4. Effect of heterogeneity

It is known that fracture propagation usually selects a path of least resistance within the material. Consequently, the heterogeneity of the rock, reflecting a random location of local strength, most strongly controls the hydraulic fracturing behavior in many ways, including fracture initiation pressure, breakdown pressure and fracture propagation path. To investigate the effect of heterogeneity, a series of simulations were conducted in which various homogeneity indices of elastic modulus (λ_m = 1.5, 2.0, 2.5, 3.0, 6.0 and 10.0) were used with principal stresses of $\sigma_1 = -6.0$ MPa and $\sigma_3 = -1.0$ MPa and a constant pressurization rate of C = 0.50 MPa/s. Only the mechanical heterogeneity is examined here, and the effect of permeability is discussed in the following subsection.

Fig. 18a presents the results of fracture initiation pressure P_i and breakdown pressure P_b for the specimens with varying levels of mechanical homogeneity (indices). The distance d_0 at which the unstable hydraulic fracture initiates under breakdown pressure is also plotted in this figure. It is demonstrated that with increasing homogeneity (identified by an increasing index) both initiation P_i and breakdown P_b pressures increase gently but d_0 drops rapidly. That is to say, for more homogenous rock a higher hydraulic pressure is required to initiate fracture and to also lead to breakdown, and moreover, the breakdown tends to take place closer to the borehole wall. Yang [19] also obtained similar results by using the RFPA-Flow code. Such an effect of heterogeneity can be explained by the rationalization that the random distribution of mechanical properties in rocks plays a leading role in fracture evolution. For more heterogonous rock, it generally contains more weaker areas (pre-existing defects) which are more likely to initiate and propagate under lower hydraulic pressure, thus having lower critical pressures (i.e. P_i and P_b). On the other hand, it is not hard to understand that more ruptured zones occur in the heterogeneous rock than homogenous rock at the same hydraulic pressure. This may explain why the distance d_0 declines with an increasing homogeneity index.

Furthermore, it is worthwhile noting that the present model is scale-dependent. In addition to the effect of the magnitude of heterogeneity variation, the hydraulic fracturing behavior depends on the spatial length scale associated with the heterogeneity. To examine the effect of the length scale of heterogeneity, a set of simulations with the same mechanical homogeneity index (λ_m = 2.5) were performed in which various sizes of the REV (L_{REV} = 0.5, 1.0, 1.25, 2.0, 3.125 and 4.0 mm) were used to discretize the problem geometry (Fig. 14a). The resulting fracture initiation pressure P_i, breakdown pressure P_b and its associated distance d_0 are shown as a function of the REV size in Fig. 18b. It is apparent that the increase in size of the REV leads to an approximately linear growth of both initiation pressure P_i and breakdown pressure P_b but a decrease of d_0. One possible reason for the increase of P_i and P_b is that, as can be seen from Fig. 15, the average effective stresses and pore pressure over the larger REV are less than those over the smaller REV under otherwise identical conditions, and hence the larger REV generally requires a higher hydraulic pressure to develop rupture. Conversely, when an identical distribution function of heterogeneity and associated parameters are adopted in the same model geometry, the rock composed of the larger REVs will include a relatively small number of weaker elements. Consequently, for rock comprising the larger REVs, fewer elements are ruptured and higher hydraulic pressures are required, which is consistent with having a higher critical pressure P_i and P_b and a lower distance d_0. It is clear that the length scale effect leads to different results. A reasonable REV size should be chosen according to the size of the fracture process zone [33,36].

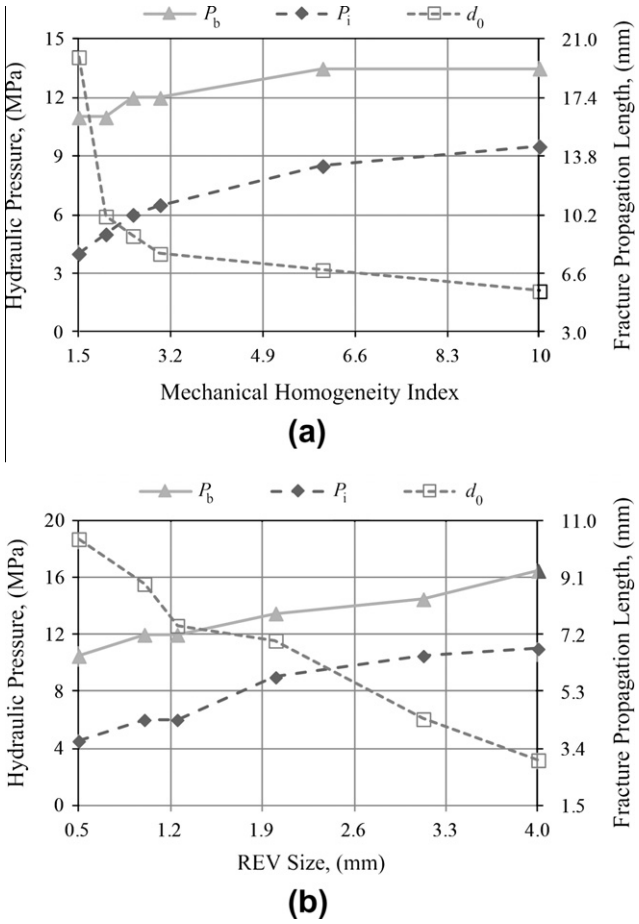

Fig. 18. Influence of (a) mechanical homogeneity index (λ_m = 1.5, 2.0, 2.5, 3.0, 6.0 and 10.0) and (b) REV size (L_{REV} = 0.5, 1.0, 1.25, 2.0, 3.125 and 4.0 mm) on fracture initiation pressure (P_i), breakdown pressure (P_b), and the distance (d_0) for unstable hydraulic fracture initiation of numerical specimens.

4.5. Effect of pressurization rate and permeability

The above discussion has demonstrated that the proposed model is capable of capturing the principal features representing hydraulic fracturing in permeable rock in a mechanistically consistent manner. Here, we focus on another interesting problem related to unusual phenomena related to the pressurization rate/permeability dependence of breakdown pressures [60,61] during hydraulic fracturing. This is a controversial and only partially re-

solved issue with regard to interpretation of the critical breakdown pressure in hydraulic fracturing.

There are two classical formulas for interpreting breakdown pressure in terms of far-field stresses and depending on the fluid pressure boundary conditions. The Hubbert–Willis (H–W) solution [57] is for "impermeable" rocks where the fluid does not penetrate the skin of the borehole wall and the Haimson–Fairhurst (H–F) solution [55] is for "permeable" rocks where the borehole skin is permeated by the injecting fluid. These different conceptualizations result in two different predictions of fracture initiation pressure representing end members of zero (H–W) and finite permeability (H–F), respectively, as:

$$\begin{cases} P_{HW} = \sigma_t - 3\sigma_3 + \sigma_1 \\ P_{HF} = \frac{\sigma_t - 3\sigma_3 + \sigma_1}{2-\alpha(1-2\nu)/(1-\nu)} \end{cases} \quad (14)$$

where P_{HW} and P_{HF} are the breakdown pressures related to the impermeable H–W and permeable H–F solutions, respectively, σ_1 and σ_3 are the far-field principal stresses ($|\sigma_1| \geqslant |\sigma_3|$, with compression considered negative), σ_t is the tensile strength of the rock. Note that Eq. (14) for the breakdown pressure is derived based on the criterion that breakdown occurs when the tangential Terzaghi effective stress at the borehole wall reaches the tensile strength of rock. But in reality, the fracture propagation after initiation could be still stable until the hydraulic pressure reaches another critical point. Consequently, the critical pressure predicted by Eq. (14) should be considered a fracture initiation pressure instead of a breakdown pressure. In addition, neither pressurization rate nor permeability is incorporated in Eq. (14), so it is unable to explain such effects on breakdown pressure or the transitional pressurization rate to permeability ratio where one solution will transit from "impermeable" to "permeable".

To explore whether the numerical model presented in this paper could replicate the effect of borehole pressurization rate and permeability on breakdown pressure, two sets of simulations are performed with various permeability and borehole pressurization rates: (i) the borehole pressurization rate is retained at $C = 0.5$ MPa/s, and the initial permeability ranges from 10^{-19} to 10^{-14} m^2; and (ii) the initial permeability is retained at $k_0 = 10^{-17}$ m^2, and different constant rates of pressurization are applied between 10^{-3} and 10^{-2} MPa/s. These correspond to a series of time increments Δt ranging from 0.005 to 500 s when the constant hydraulic pressure increment $\Delta P = 0.5$ MPa is adopted for different models. To facilitate comparison between models, the numerical specimens are assumed to be homogenous in both mechanical and hydraulic properties.

Table 4 lists the numerically-obtained tangential effective stresses acting on these first-ruptured REVs at the borehole wall for different values of pressurization rate and permeability. It is clear that all these values under a variety of conditions remain close to a mean value of $\sigma_t^M = 14.46$ MPa. This implies that the fracture initiation occurs at the same tangential effective stress σ_t^M and this value can be regarded as the tensile strength of the rock containing the borehole. Such observation conforms to an extensively used and experimentally verified criterion in the theories of hydraulic fracturing that fracturing initiation takes place as the maximum tangential effective stress at the borehole exceeds the tensile strength of the rock, which further confirms the validity of the proposed model. In addition, Table 4 also lists the theoretical values of tensile strength of the borehole (σ_t^{HW} and σ_t^{HF}) evaluated from the H–W solution and H–F solution (Eq. (14)) with different fracture initiation pressures. It is seen that the H–F solution overestimates the tensile strength of the borehole while the H–W solution underestimates that value. However, this error deceases for the H–F solution in the case of higher permeability or lower pressurization rate and for the H–W solution in the case of lower permeability or higher pressurization rate. This infers that the H–F solution and H–W solution are derived accurately from the two extremes of "permeable" rocks and "impermeable" rocks, respectively. But compared with these theoretical solutions, the proposed numerical model predicts the tensile strength of the borehole with sufficient accuracy from the microscopic standpoint using a microcrack propagation criterion instead of a macroscopic fracturing criterion related to the tensile strength.

Table 4
Tensile strength of the borehole evaluated from the numerical simulation and the conventional theories (H–F solution [57] and H–W solution [55]) for different permeability and pressurization rates.

Permeability (m^2)	Evaluated tensile strength (MPa)		
	Numerical simulation	H–F solution	H–W solution
1E−19	14.16	18.16	13.50
5E−19	14.37	18.16	13.50
1E−18	14.45	18.16	13.50
5E−18	14.07	17.44	13.00
1E−17	14.26	17.44	13.00
5E−17	14.76	16.72	12.50
1E−16	14.64	15.99	12.00
5E−16	14.87	14.55	11.00
1E−15	14.61	13.83	10.50
1E−14	14.86	13.83	10.50
Pressurization rate (MPa/s)			
1E−3	14.26	13.83	10.50
5E−3	14.61	13.83	10.50
1E−2	14.86	14.55	11.00
5E−2	14.64	15.99	12.00
1E−1	14.76	16.72	12.50
5E−1	14.26	17.44	13.00
1E0	14.07	17.44	13.00
5E0	14.45	18.16	13.50
1E1	14.37	18.16	13.50
5E1	14.16	18.16	13.50
1E2	14.01	18.16	13.50
Average	14.46	16.51	12.36

Fig. 19 shows the simulated results of fracture initiation pressure and breakdown pressure as a function of borehole pressurization rate and permeability. It is seen that the transition of the two critical hydraulic pressures from one regime (lower pressurization rate/permeability) to another (higher pressurization rate/permeability) are well replicated by the present numerical model. With the increase of pressurization rate, the simulated breakdown pressure tends to increase (see Fig. 19a), which is in agreement with typical experimental observations [60,61]. Moreover, it is shown in Fig. 19a that the simulated initiation pressure first remains largely unchanged in the lower pressurization rate regime ($<10^{-2}$ MPa/s), then approximately linearly increases with the pressurization rate, until it finally remains constant in the higher pressurization rate regime ($>10^{1}$ MPa/s). Interestingly, the H–W solution for "impermeable" rocks and H–F solution for "permeable" rocks (see Eq. (14)) comprise the lower and upper limit of the simulated initiation pressure, respectively, as shown by the two dashed lines in Fig. 19a. Such results are consistent with the previous theoretical investigation [56]. This may also imply that the proposed two-scale model has a unique ability to provide deep insight into the effect of fluid permeation on the hydraulic fracturing behavior.

Furthermore, Fig. 19b clearly shows the numerically-obtained evolution of two critical hydraulic pressures with permeability. This numerical approach provides a useful virtual experimental tool to verify the theoretical models. From Fig. 19b it is apparent that both initiation pressure and breakdown pressure generally decrease with permeability. In particular, the simulated initiation pressure in the lower permeability regime ($<10^{-18}$ m^2) approaches the H–W solution (for "impermeable" rocks) while that in the

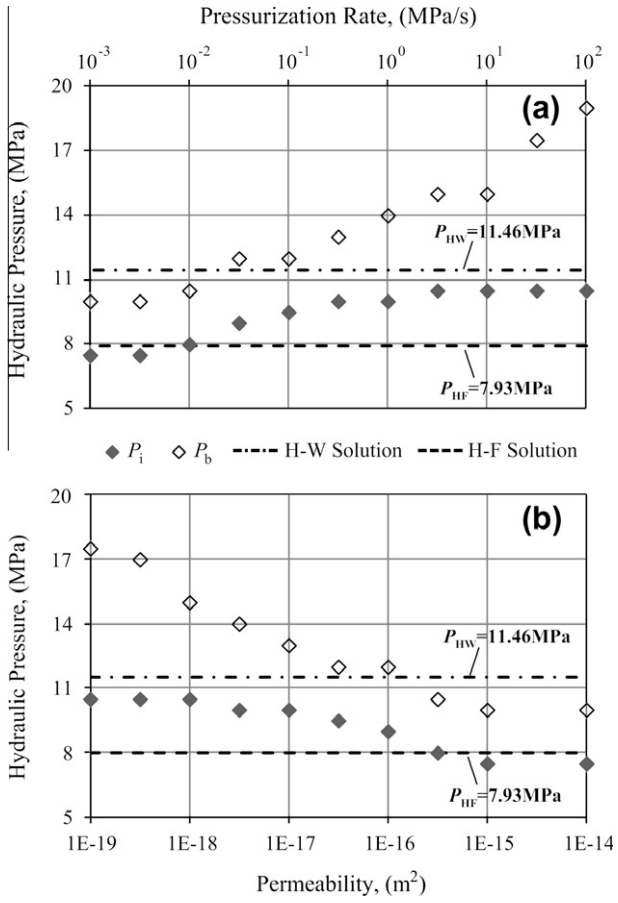

Fig. 19. Influence of pressurization rate and permeability on fracture initiation pressure (P_i) and breakdown pressure (P_b). P_{HW} and P_{HF} are the critical pressures evaluated from H–W [57] solution and H–F solution [55] with the average tensile strength in Table 4, respectively.

higher permeability regime (>10^{-15} m^2) is close to the H–F solution (for "permeable" rocks). The simulation results demonstrate the validity of these two classical formulae (Eq. (14)) representing two extremes in permeability magnitudes. More importantly, the natural transition of hydraulic fracturing behavior in rock from "impermeable" to "permeable" are reproduced by the proposed model in a physically realistic manner.

The achievements of the present model may be attributed to the conceptual model of fracturing in which the REV of the rock, intrinsic to this model, is proposed to characterize an element where fracturing may occur. The pressurization-rate-dependent and permeability-dependent critical hydraulic pressures shown in Fig. 19 may be interpreted using the conjecture based on the proposed model that the higher permeability causes the fluid to more rapidly penetrate into the rock surrounding the borehole and that the lower pressurization rate also allows the wider spread of fluid in the rock due to the extended duration of injection. Both the higher permeability and lower pressurization rate would elevate the average pore pressure and the average effective stresses over the REVs of rock in the vicinity of the borehole, and thus lead to the rupture of these REVs at the lower hydraulic pressure. Moreover, the sufficiently lower permeability and higher pressurization rate would cause an extremely small distance of fluid penetration from the borehole. Conversely, fluid penetration would be considerable and tend to be steady surrounding the borehole in the case of sufficiently higher permeability and lower pressurization rate. Both of the two extremes would result in a slight change in the average pore pressure and the average effective stresses over the REVs of rock around the borehole. This may explain why the simulated initiation pressure in the lower permeability/higher pressurization rate regime or the higher permeability/lower pressurization rate regime remains largely unchanged.

5. Conclusions

The modeling of coupled evolution of fractures and fluid flow remains an important topic in a variety of rock engineering problems. Continuum numerical methods are predominant in the modeling of rock engineering practice problems, but their capacities are limited in simulating the problem of fracturing evolution coupled by fluid flow. There is a requirement for them to be extended to adequately accommodate such coupled behavior. Motivated by this, we present an approach based on a two-scale conceptual model representing rocks containing flaws and in the framework of a continuum method to model the interaction between the fracture evolution and extension coupled with fluid flow. This approach combines a microcrack-based continuous damage model with generalized Biot poroelasticity. The macroscopic elastic tensors of stiffness, Biot effective stress coefficient as well as that of overall permeability are directly related to the microstructural microcrack kinetics. This approach overcomes the disadvantages encountered in the previous phenomenological hydro-mechanical coupling models [20,21]. The proposed modeling approach allows the prediction of the transition from random microcracking to macroscopic localized fracturing together with the evolution of fluid flow in permeable rocks during processes of hydro-mechanical interaction.

Examining the response of a single elementary REV with varying confining pressures and fluid pressures demonstrates the basic nature of the proposed model. The numerical results show that the confining pressure increases both the ultimate strength and the strain hardening range but that elevated pore pressure decreases them. It is also apparent that the major damage is accumulated in the direction perpendicular to the loading axis. Such anisotropic damage causes the permeability in the loading direction and the lateral Biot effective stress coefficient to increase but the lateral modulus to deteriorate. The permeability at the peak stress state is increased by nearly three orders of magnitude relative to the initial permeability. These general characteristics, replicated by the proposed model, are in good agreement with reported experimental observations [45].

Simulations of standard biaxial compression experiments further verify the general macroscopic behavior of the coupled damage and flow model. Heterogeneity in both mechanical and hydraulic properties is introduced in the model to simulate localized failure. The simulation results replicate typical experimental observations including the complete stress–strain relation, permeability evolution, acoustic emission (AE) rates and failure modes. Initial heterogeneity strongly influences the resulting fracture patterns and flow paths. The more heterogeneous rocks show more ductile post-failure behavior, lower peak strength and permeability, and more complex fracture patterns. Another notable observation is that the presence of the resulting macroscopic shear fracture is well reproduced by the proposed model in which only a Mode I fracture criterion is employed. The macroscopic shear fracture results from the coalescence of multiple tensile microcracks congruent with common interpretations of shear failure [49]. However, since no shear strength criterion is applied to the contacting faces of flaws within the damage zone, no prediction of shear-band orientation is possible.

Finally, the proposed modeling approach is applied to simulate hydraulic fracturing in permeable rocks. Fracture propagation driven by hydraulic pressure is examined from the viewpoint of coupled damage-flow interactions. The simulation results indicate that

the proposed model is capable of reproducing the evolution of hydraulic fracturing and fluid flow in permeable rocks in a physically realistic manner. This conceptualization is capable of representing the two critical pressures, i.e. fracture initiation pressure and breakdown pressure, during the hydraulic fracturing process. The fracture initiation pressure is lower than the breakdown pressure and the unstable hydraulic fracture only initiates under breakdown pressure at a point distant from the borehole wall. The effects of heterogeneities, length scale of the REV, rock permeability and borehole pressurization rate on critical pressures are also examined. It is found that more homogenous rock or the rock composed of the smaller REVs requires lower hydraulic pressure to initiate fracture and breakdown. Moreover, both the initiation pressure and breakdown pressure decrease with the permeability but increase with the pressurization rate, and the theoretical impermeable wall (H–W) and permeable wall (H–F) solutions give the upper and lower limit of the initiation pressure, respectively. Such numerical results are consistent with experimental observations [60,61] and theoretical results [56].

In summary the presented microcrack-based damage and flow coupled model is capable of predicting the evolution of fracturing and fluid flow in permeable rocks, inclusive of key processes at microscale, in a physically realistic manner. It can be successfully applied to a variety of hydro-mechanical problems in practical rock engineering.

Appendix A

For the 2-D plane strain problem ($D_{i3} = D_{3i} = 0$), the damaged elastic modulus tensor $\mathbf{C}(\mathbf{D})$ can be expanded to the following matrix form:

$$\begin{bmatrix}\sigma_{11}\\ \sigma_{22}\\ \sigma_{33}\\ \sigma_{12}\end{bmatrix} = \begin{bmatrix} \lambda+\mu+2AD_{11}+4BD_{11} & \lambda+A[D_{22}+D_{11}] & \lambda+AD_{11} & 2(AD_{12}+2BD_{12}) \\ \lambda+A[D_{22}+D_{11}] & \lambda+2\mu+2AD_{22}+4BD_{22} & \lambda+AD_{22} & 2(AD_{12}+2BD_{21}) \\ \lambda+AD_{11} & \lambda+AD_{22} & \lambda+2\mu & 2AD_{12} \\ AD_{12}+2BD_{12} & AD_{12}+2BD_{21} & AD_{12} & 2\mu+2B[D_{22}+D_{11}] \end{bmatrix} \begin{bmatrix}\varepsilon_{11}\\ \varepsilon_{22}\\ 0\\ \varepsilon_{12}\end{bmatrix} \tag{A1}$$

The components of Biot effective stress coefficients tensor $\boldsymbol{\alpha}(\mathbf{D})$ are expanded as follows:

$$\begin{cases} \alpha_{11} = 1 - \frac{3\lambda+2\mu+4(A+B)D_{11}+AD_{22}}{3K_s} \\ \alpha_{22} = 1 - \frac{3\lambda+2\mu+(A+B)D_{22}+AD_{11}}{3K_s} \\ \alpha_{12} = \alpha_{21} = -\frac{(3A+4B)D_{12}}{3K_s} \end{cases} \tag{A2}$$

Similarly, Biot modulus $M(\mathbf{D})$ is expressed as:

$$M = \frac{K_s}{\left(1 - \frac{9\lambda+6\mu+(6A+4B)(D_{11}+D_{22})}{81K_s}\right) - \phi\left(1 - \frac{K_s}{K_f}\right)} \tag{A3}$$

References

[1] Rutqvist J, Stephansson O. The role of hydromechanical coupling in fractured rock engineering. Hydrogeol J 2003;11(1):7–40.
[2] Gueguen Y, Dienes J. Transport properties of rocks from statistics and percolation. Math Geol 1989;21(1):1–13.
[3] Benson P, Schubnel A, Vinciguerra S, Trovato C, Meredith P, Young RP. Modeling the permeability evolution of microcracked rocks from elastic wave velocity inversion at elevated isostatic pressure. J Geophys Res – Solid Earth 2006;111(B4).
[4] Wong RHC, Chau KT, Wang P. Microcracking and grain size effect in Yuen Long marbles. Int J Rock Mech Min Sci Geomech Abstr 1996;33(5):479–85.
[5] Sprunt ES, Brace WF. Direct observation of microcavities in crystalline rocks. Int J Rock Mech Min 1974;11(4):139–50.
[6] Kranz RL. Microcracks in rocks: a review. Tectonophysics 1983; 100(1–3):449–80.
[7] Jing L. A review of techniques, advances and outstanding issues in numerical modelling for rock mechanics and rock engineering. Int J Rock Mech Min 2003;40(3):283–353.
[8] Yuan SC, Harrison JP. A review of the state of the art in modelling progressive mechanical breakdown and associated fluid flow in intact heterogeneous rocks. Int J Rock Mech Min 2006;43(7):1001–22.
[9] Potyondy DO, Cundall PA. A bonded-particle model for rock. Int J Rock Mech Min 2004;41(8):1329–64.
[10] Schlangen E, Garboczi E. Fracture simulations of concrete using lattice models: computational aspects. Eng Fract Mech 1997;57(2–3):319–32.
[11] Blair SC, Cook NGW. Analysis of compressive fracture in rock using statistical techniques: Part I. A non-linear rule-based model. Int J Rock Mech Min 1998;35(7):837–48.
[12] Blair SC, Cook NGW. Analysis of compressive fracture in rock using statistical techniques: Part II. Effect of microscale heterogeneity on macroscopic deformation. Int J Rock Mech Min 1998;35(7):849–61.
[13] Reuschle T. A network approach to fracture: the effect of heterogeneity and loading conditions. Pure Appl Geophys 1998;152(4):641–65.
[14] Potyondy DO, Cundall PA, Lee CA. Modelling rock using bonded assemblies of circular particles. In: Aubertin M, Hassani F, Mitri H, editors. Rock mechanics tools and techniques, Vols. 1 and 21996. p. 1937–44.
[15] Schlangen E, Garboczi E. New method for simulating fracture using an elastically uniform random geometry lattice. Int J Eng Sci 1996;34(10): 1131–44.
[16] Krajcinovic D. Damage mechaincs. Mech Mater 1989;8(2–3):117–97.
[17] Tang CA. Numerical simulation of progressive rock failure and associated seismicity. Int J Rock Mech Min 1997;34(2):249–61.
[18] Fang Z, Harrison JP. Development of a local degradation approach to the modelling of brittle fracture in heterogeneous rocks. Int J Rock Mech Min 2002;39(4):443–57.
[19] Yang TH, Tham LG, Tang CA, Liang ZZ, Tsui Y. Influence of heterogeneity of mechanical properties on hydraulic fracturing in permeable rocks. Rock Mech Rock Eng 2004;37(4):251–75.
[20] Tang CA, Tham LG, Lee PKK, Yang TH, Li LC. Coupled analysis of flow, stress and damage (FSD) in rock failure. Int J Rock Mech Min 2002;39(4):477–89.
[21] Yuan SC, Harrison JP. Development of a hydro-mechanical local degradation approach and its application to modelling fluid flow during progressive fracturing of heterogeneous rocks. Int J Rock Mech Min 2005;42(7–8):961–84.
[22] Lyakhovsky V, Hamiel Y. Damage evolution and fluid flow in poroelastic rock. Izv Phys Solid Earth 2007;43(1):13–23.
[23] Guéguen Y. Mechanics of fluid saturated rocks. Academic Press; 2004.
[24] Oda M, Katsube T, Takemura T. Microcrack evolution and brittle failure of Inada granite in triaxial compression tests at 140 MPa. J Geophys Res 2002;107(B10):; 23.
[25] Hu D, Zhou H, Zhang F, Shao JF. Evolution of poroelastic properties and permeability in damaged sandstone. Int J Rock Mech Min 2010;47(6): 962–73.
[26] Costin L. A microcrack model for the deformation and failure of brittle rock. J Geophys Res 1983;88(B11):9485–92.
[27] Costin L. A finite element material model for microfracture-damaged brittle rock. Albuquerque, NM (USA): Sandia National Labs; 1988.
[28] Homand-Etienne F, Hoxha D, Shao JF. A continuum damage constitutive law for brittle rocks. Comput Geotech 1998;22(2):135–51.
[29] Shao JF. Poroelastic behaviour of brittle rock materials with anisotropic damage. Mech Mater 1998;30(1):41–53.
[30] Shao JF, Zhou H, Chau K. Coupling between anisotropic damage and permeability variation in brittle rocks. Int J Numer Anal Methods 2005;29(12):1231–47.
[31] Souley M, Homand F, Pepa S, Hoxha D. Damage-induced permeability changes in granite: a case example at the URL in Canada. Int J Rock Mech Min 2001;38(2):297–310.
[32] Golshani A, Okui Y, Oda M, Takemura T. A micromechanical model for brittle failure of rock and its relation to crack growth observed in triaxial compression tests of granite. Mech Mater 2006;38(4):287–303.
[33] Mazars J, Pijaudier-Cabot G. From damage to fracture mechanics and conversely: a combined approach. Int J Solids Struct 1996;33(20):3327–42.
[34] Costin LS. Damage mechanics in the post-failure regime. Mech Mater 1985;4(2):149–60.
[35] Zhu WC, Tang CA. Micromechanical model for simulating the fracture process of rock. Rock Mech Rock Eng 2004;37(1):25–56.
[36] Bažant ZP, Oh B. Crack band theory for fracture of concrete. Mater Struct 1983;16(3):155–77.
[37] Shao JF, Lu Y, Lydzba D. Damage modeling of saturated rocks in drained and undrained conditions. J Eng Mech 2004;130:733.
[38] Cheng AHD. Material coefficients of anisotropic poroelasticity. Int J Rock Mech Min 1997;34(2):199–205.

[39] Halm D, Dragon A. A model of anisotropic damage by mesocrack growth; unilateral effect. Int J Damage Mech 1996;5(4):384–402.
[40] Kachanov M. Effective elastic properties of cracked solids: critical review of some basic concepts. ASME Appl Mech Rev 1992;45(8):304–35.
[41] Shao JF, Hoxha D, Bart M, Homand F, Duveau G, Souley M, et al. Modelling of induced anisotropic damage in granites. Int J Rock Mech Min 1999;36(8): 1001–12.
[42] Horii H, Nematnasser S. Brittle failure in compression: splitting, faulting and brittle–ductile transition. Philos Trans Royal Soc London Ser A – Math Phys Eng Sci 1986;319(1549):337–74.
[43] Tham LG, Li L, Tsui Y, Lee PKK. A replica method for observing microcracks on rock surfaces. Int J Rock Mech Min 2003;40(5):785–94.
[44] Detournay E, Cheng AHD. Fundamentals of poroelasticity. In: Comprehensive rock engineering: principles PaP, editor. Analysis and design method. Pergamon, 1993. p. 113–71.
[45] Oda M, Takemura T, Aoki T. Damage growth and permeability change in triaxial compression tests of Inada granite. Mech Mater 2002;34(6): 313–31.
[46] Arson C, Pereira JM. Influence of damage on pore size distribution and permeability of rocks. Int J Numer Anal Methods 2012.
[47] Wang JA, Park H. Fluid permeability of sedimentary rocks in a complete stress–strain process. Eng Geol 2002;63(3):291–300.
[48] Lockner D. The role of acoustic emission in the study of rock fracture. Int J Rock Mech Min Sci Geomech Abstr 1993;30:883–99.
[49] Broberg K. On crack paths. Eng Fract Mech 1987;28(5–6):663–79.
[50] Zhu WL, Wong TF. Network modeling of the evolution of permeability and dilatancy in compact rock. J Geophys Res – Solid Earth 1999;104(B2): 2963–71.
[51] Yang T, Zhu W, Yu Q, Liu H. The role of pore pressure during hydraulic fracturing and implications for groundwater outbursts in mining and tunnelling. Hydrogeol J 2011:1–14.
[52] Detournay E. Propagation regimes of fluid-driven fractures in impermeable rocks. Int J Geomech 2004;4(1):35.
[53] Adachi J, Siebrits E, Peirce A, Desroches J. Computer simulation of hydraulic fractures. Int J Rock Mech Min 2007;44(5):739–57.
[54] Detournay E, Cheng AHD. Poroelastic response of a borehole in a non-hydrostatic stress field. Int J Rock Mech Min Sci Geomech Abstr 1988;25(3): 171–82.
[55] Haimson B, Fairhurst C. Initiation and extension of hydraulic fractures in rocks. Old SPE J 1967;7(3):310–8.
[56] Detournay E, Cheng A. Influence of pressurization rate on the magnitude of the breakdown pressure. In: Proceedings of 33rd US rock mechanics symposium, Balkema, Rotterdam 1992. p. 325–33.
[57] Hubbert MK, Willis DG. Mechanics of hydraulic fracturing. AIME Petrol Trans 1957;210:153–68.
[58] Garagash D, Detournay E. An analysis of the influence of the pressurization rate on the borehole breakdown pressure. Int J Solids Struct 1997;34(24): 3099–118.
[59] Ito T. Effect of pore pressure gradient on fracture initiation in fluid saturated porous media: rock. Eng Fract Mech 2008;75(7):1753–62.
[60] Haimson B, Fairhurst C. In-situ stress determination at great depth by means of hydraulic fracturing. In: Proceedings of the eleventh US symposium on rock mechanics, Berkeley; 1969. p. 559–84.
[61] Zoback M, Rummel F, Jung R, Raleigh C. Laboratory hydraulic fracturing experiments in intact and pre-fractured rock. Int J Rock Mech Min Sci 1977;14:49–58.